

# Strong nebular He II emission induced by He<sup>+</sup> ionizing photons escaping through the clumpy winds of massive stars

A. Roy<sup>1,2\*</sup>, M. R. Krumholz<sup>2,3</sup>, S. Salvadori<sup>4,5</sup>, G. Meynet<sup>6,7</sup>, S. Ekström<sup>6,7</sup>, J. S. Vink<sup>8</sup>, A. A. C. Sander<sup>9</sup>, R. S. Sutherland<sup>2,3</sup>, S. Paul<sup>10,11,12</sup>, A. Pallottini<sup>1</sup>, and Á. Skúladóttir<sup>4,5</sup>

<sup>1</sup> Scuola Normale Superiore, Piazza dei Cavalieri 7, I-56126 Pisa, Italy

<sup>2</sup> Research School of Astronomy and Astrophysics, Australian National University, Cotter Road, Weston Creek, ACT 2611, Australia

<sup>3</sup> ARC Centre of Excellence for All Sky Astrophysics in 3 Dimensions (ASTRO 3D), Canberra, ACT 2611, Australia

<sup>4</sup> Dipartimento di Fisica e Astronomia, Università degli Studi di Firenze, via G. Sansone 1, 50019, Sesto Fiorentino, Italy

<sup>5</sup> INAF - Osservatorio Astrofisico di Arcetri, Largo E. Fermi 5, I-50125, Firenze, Italy

<sup>6</sup> Département d’Astronomie, Université de Genève, Chemin Pegasi 51, CH-1290 Versoix, Switzerland

<sup>7</sup> Gravitational Wave Science Center (GWSC), Université de Genève, CH-1211 Geneva, Switzerland

<sup>8</sup> Armagh Observatory and Planetarium, Armagh, Northern Ireland, BT61 9DG

<sup>9</sup> Zentrum für Astronomie der Universität Heidelberg, Astronomisches Rechen-Institut, Mönchhofstr. 12-14, 69120 Heidelberg

<sup>10</sup> Jodrell Bank Centre for Astrophysics, School of Physics and Astronomy, The University of Manchester, Manchester M13 9PL, UK

<sup>11</sup> Department of Physics, McGill University, Montreal, QC, Canada H3A 2T8

<sup>12</sup> Department of Physics and Astronomy, University of the Western Cape, Robert Sobukhwe Road, Bellville, 7535, South Africa

Received XXX / Accepted YYY

## ABSTRACT

**Context.** The origin of nebular He II emission in both local and high-redshift galaxies remains an unsolved problem. Various theories have been proposed to explain it, including He II-ionizing photons produced by high mass X-ray binaries, ultra-luminous X-ray sources, or “stripped” He stars produced by binary interaction or evolution of rapidly rotating ( $v/v_{\text{crit}} \gg 0.4$ ) single massive stars, shock ionization, and hidden active galactic nuclei. All these theories have shortcomings, however, leaving the cause of nebular He II emission unclear.

**Aims.** We investigate the hypothesis that the photons responsible for driving nebular He II emission are produced by evolution of single massive stars and/or Wolf-Rayet (WR) star whose winds are on the verge of becoming optically thin due to clumping, allowing significant escape of hard ionizing photons. We combine models of stellar evolution with population synthesis and nebular models to identify the most favorable scenarios for producing nebular He II via this channel.

**Methods.** We use the Modules for Experiments in Stellar Astrophysics (MESA) code to compute evolutionary tracks for stars with initial masses 10 – 150  $M_{\odot}$  and a range of initial metallicities and rotation rates. We then combine these tracks with a range of custom treatments of stellar atmospheres, intended to capture the effects of clumping, in the population synthesis code Stochastically Lighting Up Galaxies (SLUG) to produce the total ionizing photon budgets and spectra. We use these spectra as inputs to CLOUDY calculations of nebular emission at a range of nebular densities and metallicities.

**Results.** We find that, if WR winds are clumpy enough to become close to optically thin, stellar populations with a wide range of metallicities and rotation rates can produce He II ionizing photons at rates sufficient to explain the observed nebular  $I(\text{He II})/I(\text{H}\beta)$  ratio  $\sim 0.004 - 0.07$  found in He II-emitting galaxies. Metal-poor, rapidly rotating stellar populations ( $[\text{Fe}/\text{H}] = -2.0$ ,  $v/v_{\text{crit}} = 0.4$ ) also reach these levels of He II production even for partially clumpy winds. These scenarios also yield He II, H $\beta$ , and “Blue-Bump” line equivalent widths comparable to those observed in He II emitters. Only for laminar, non-clumpy winds, do we fail to find combinations of metallicity and stellar rotation rate that yield  $I(\text{He II})/I(\text{H}\beta)$  values as high as those observed in He II-emitters.

**Conclusions.** Contrary to previous findings, we conclude that single WR stars can be a strong source for nebular He II emission if their winds are sufficiently clumpy. This scenario also reproduces a range of other properties found in He II emitters, suggesting that hard photons escaping through clumpy WR winds are a strong candidate to explain nebular He II-emission.

**Key words.** stars: abundances – stars: massive – stars: mass-loss – ISM: abundances – galaxies: evolution – galaxies: ISM

## 1. Introduction

The He II  $\lambda 4686$  and He II  $\lambda 1640$  emission lines that are commonly observed in the optical and UV spectra of active galactic nuclei (AGN) and star-forming (SF) galaxies result from the recombination of He<sup>++</sup> with e<sup>-</sup>. Production of these lines therefore requires the presence of hard ionizing photons at energies  $\geq 54.4$

eV, or wavelengths  $\lambda \leq 228 \text{ \AA}$ , corresponding to the ionization potential of singly ionized He. The presence of such hard photons is expected in galaxies that host an AGN. However, both direct observations and indirect inferences from population studies indicate that SF galaxies also manage to produce photons at these energies. Directly, nebular He II emission has been detected in SF galaxies without any AGN signatures, particularly at sub-solar metallicities for local galaxies, and in galaxies at redshifts

\* e-mail: arpita.roy1016@gmail.com

$z \gtrsim 2$  (Shirazi & Brinchmann 2012; James et al. 2022). Indirectly, AGN number density drops sharply at redshifts  $z \gtrsim 3$ , while He II emitters are found up to  $z \sim 7$  (Cassata et al. 2013; Stark 2016; Patrício et al. 2016; Berg et al. 2018; Sobral et al. 2019; Nanayakkara et al. 2019; Saxena et al. 2020a). He II emitters indeed become increasingly prevalent at higher redshifts: Kehrig et al. (2011, 2016) found that  $\gtrsim 3\%$  of the galaxy population at  $z \gtrsim 3$  exhibits narrow He II lines, well above the fraction ( $\sim 1 - 1.5\%$ ) at  $z \sim 0$  (Saxena et al. 2020a). The combination of a drop in AGN number density with an increase in He II emitter fraction at high redshift means that AGNs are unlikely to be significant contributors to He II emission at  $z \gtrsim 3$  (Feltre et al. 2016 and references therein).

While this evidence strongly suggests that SF galaxies can in at least some circumstances produce photons well past the He<sup>+</sup> ionization edge, the precise origin of He II emission in SF galaxies is poorly understood. One possible route is through the production of compact objects at the ends of massive stars' lives. In support of this hypothesis, many local ( $z \sim 0$ ) galaxies exhibiting robust He II  $\lambda 4686$  emission are characterized by low metallicities, as exemplified by I Zw18, SBS0335-052E with a metallicity of  $Z \sim 1/30, Z_{\odot}$  (Kehrig et al. 2016, 2018), or the young massive cluster NGC 346 (Sixtos et al. 2023 and references therein) in the Small Magellanic Cloud (SMC). This is a significant clue because X-ray luminosity per unit star-formation rate ( $L_X/\text{SFR}$ ) and He II  $\lambda 4686$  intensity display a strikingly similar anti-correlation with metallicity, which led Schaerer et al. (2019) to suggest that high-mass X-ray binaries (HMXB) and/or ultra-luminous X-ray (ULX) sources serve as the primary contributors to nebular He II emission. Schaerer et al.'s hypothesis is also supported by the fact that HMXBs are observed to be produced more readily in metal-poor stellar populations. Consistent with this scenario, Mayya et al. (2023) found that, of 32 He II  $\lambda 4686$  emitting H II-regions in the Cartwheel galaxy (which has an LMC-like metallicity), 10 coincide with ULX sources.

However, Senchyna et al. (2020) argue that HMXBs are insufficiently luminous by themselves to explain observed He II line strengths, and suggest as an alternative modifications to stellar wind prescriptions (which affect massive stellar hard ionizing photon budgets) and/or additional softer X-ray sources alongside HMXBs. In support of this argument, Saxena et al. (2020b) found no significant difference between the X-ray luminosities and  $L_X/\text{SFR}$  ratios of 18 He II  $\lambda 1640$ -emitting SF galaxies selected from the VANDELS survey at  $z \approx 2 - 4$  and a control sample of non-He II emitters at similar redshifts. They conclude from this that HMXBs and/or any weak or obscured AGNs might not be the dominant He II producers at  $z \gtrsim 2$ .

Several alternative physical mechanisms have also been proposed by various authors. Ionization by strong shocks (Dopita & Sutherland 1996; Izotov et al. 2012) is one possibility, though Thuan & Izotov (2005) and Izotov et al. (2012) argue that this mechanism is viable only if shocks are so strong that they also supply  $\sim 10\%$  of the total number of hydrogen ionizing photons produced in a galaxy. However, there is currently no model establishing a quantitative connection between shock strengths and other galaxy properties, nor is it clear how a shock-driven model could explain the anti-correlation between He II emissivity and metallicity in nearby SF galaxies. Another alternative route is via the production of stars with higher effective temperatures, and thus harder ionizing spectra, than are found in standard stellar evolution models; such stars could potentially be produced via rotation-induced chemical mixing (Szécsi et al. 2015; Roy et al. 2020), through the rejuvenation of old stars through binary interactions (Eldridge et al. 2017; Götzberg et al. 2018, 2019), or

as a late stage in the evolution of metal-free population III stars (Tumlinson & Shull 2000; Schaerer 2003; Visbal et al. 2015). However, more recent quantitative explorations of the idea that "rejuvenated" stars produced by binary interactions explain He II emission have found that they are insufficient to reproduce the observed He II intensity in subsolar local galaxies (Stanway & Eldridge 2019).

Wolf-Rayet (WR) stars represent yet another possible route to He II emission. The WR phase in a massive star's life begins, in general, during the core He burning phase (e.g., Roy et al. 2020, 2021), and during it stars reach the high effective temperatures,  $T_{\text{eff}} \sim 80 - 100$  kK, required to produce photons capable of ionizing He<sup>+</sup> (Schaerer 2002). As with the HMXB scenario, this idea receives observational support from an observed correlation between He II emission and spectral features indicating a strong spectral contribution from WR stars. Some nearby SF galaxies emitting He II  $\lambda 4686$  display a "blue bump" in their spectra, a distinctive signature of the presence of WR stars that is associated with the He II  $\lambda 4686$  line blended with either N III  $\lambda 4640$  in WN stars and/or C III/C IV  $\lambda 4650$  in WC stars (Guseva et al. 2000; López-Sánchez & Esteban 2010; Kehrig et al. 2016; Mayya et al. 2020, 2023). He II emitting galaxies also occasionally exhibit a "red bump" as well (López-Sánchez & Esteban 2010), which is linked to the broad C IV  $\lambda 5808$  line primarily observed in WC stars. The  $I(\text{He II } \lambda 4686)/I(\text{H}\beta)$  ratio (here onwards abbreviated to  $I(\text{He II})/I(\text{H}\beta)$ ) in galaxies with sub-solar metallicity that show prominent WR features in their integrated spectra is a few percent (Izotov & Thuan 2004), much higher than is typical of galaxies lacking WR features. On smaller scales, Mayya et al. (2023) measured  $I(\text{He II})/I(\text{H}\beta) \sim 0.004 - 0.07$ , with a mean of  $0.01 \pm 0.003$  for the 32 He II  $\lambda 4686$  emitting H II regions in the Cartwheel galaxy.

However, the WR idea has proven difficult to test for both observational and theoretical reasons. Observationally, the problem has partly been one of resolution: most early attempts to explain He II features in spectra have focused on spectra from the Sloan Digital Sky Survey (SDSS), which typically encompass regions spanning several kiloparsecs around galactic centers. Over such large spatial scales, many physical mechanisms may contribute to He II emission, including photoionization by single and/or binary stellar populations, strong shock-driven ionization, He<sup>+</sup> ionization by "stripped" He stars, HMXBs, and even the ionization by weak AGNs. The poor resolution makes it challenging to disentangle these processes and check stellar population models against observations. For example, a number of authors have found that stellar population models fail to reproduce the observed amount of He II flux in these integrated galaxy spectra (e.g., Plat et al. 2019; Schaerer et al. 2019; Stanway & Eldridge 2019), but this may simply be because on kpc scales the spectra also contain significant contributions from SN-driven shock ionization (Plat et al. 2019).

Observations focused on individual nebulae on few hundred pc scales represent a more promising way of testing WR models (and other models where He II is driven partly by young stellar populations). However, even this approach has proven challenging. For example even with  $\sim 500$  pc observations of the metal-poor ( $Z \sim 0.03 Z_{\odot}$ ) nearby galaxy SBS 0335-052E using optical VLT/MUSE spectroscopic and Chandra X-ray observations, Kehrig et al. (2018) failed to reach any solid conclusion as to the origin of He II emission. Their findings indicated only that the observed He II ionization budget could be produced either by single rotating metal-free ( $Z \lesssim 10^{-5} Z_{\odot}$ ) stars or by a metal-poor ( $Z \sim 0.01 Z_{\odot}$ ) binary population with a top-heavy initial mass function (IMF). Kehrig et al. (2015) conclude that WR stars are

insufficient to explain the rate of He<sup>+</sup> ionization demanded by their observations of another metal-poor nearby galaxy, IZw 18. By contrast, Mayya et al. (2020) carry out MEGARA observations of the central starburst cluster in NGC 1569 and conclude that WR stars can produce enough He<sup>+</sup> ionizing photons to explain the observed He II  $\lambda$ 4686 flux. Mayya et al. (2023) reach similar conclusions from  $\sim 120$  pc resolution MUSE observations of regions around super star clusters ( $M_* \sim 10^5 - 10^7 M_\odot$ ) in the Cartwheel Galaxy.

On the theoretical side, the WR scenario has proven challenging to test because of uncertainties on the He<sup>+</sup>-ionizing fluxes of WR stars. The largest uncertainty in these models concerns the atmospheres of these stars, with almost all work published to date assuming a spherical, homogeneous, optically thick WR atmosphere. Such models are clearly inconsistent with observations that suggest that the hot winds of most WR stars consist of stochastic clumps (Schumann & Seggewiss 1975; Moffat et al. 1988; Eversberg et al. 1998; Grosdidier et al. 2001; Lépine & Moffat 2008; Chené et al. 2020), rather than having a homogeneous structure. Theoretical models predict that clumpiness significantly reduces wind mass-loss (Puls et al. 2006; Fullerton et al. 2006) compared to previous estimates (Nugis & Lamers 2000), and Sander et al. (2023) finds that if clumpiness reduced the mass loss rate below a characteristic value  $\log[\dot{M}/(M_\odot \text{ yr}^{-1})] \approx -4.5$  WR winds become transparent to He<sup>+</sup>-ionizing photons, potentially greatly increasing the escape of such photons into the ISM. However, neither the mass-loss of WR winds nor the wind opacity and/or clumpiness are well-quantified.

Our goal in this paper is to revisit the hitherto unsolved problem of nebular He II emission and demonstrate that incorporating close to optically thin and/or higher clumpiness and porous WR atmosphere models (e.g., Nugis & Lamers 2000; Vink et al. 2001) can significantly enhance the production of He<sup>+</sup> ionizing photons. Models with this new atmosphere treatment can explain both the observed He II flux as well as the  $I(\text{He II})/I(\text{H}\beta)$  ratio in H II regions through the single stellar population channel. Importantly, this explanation avoids the need to invoke additional physical mechanisms such as binarity, “stripped” He stars, shock ionization, HMXBs and/or contribution from AGNs. In addition to this primary result, we provide the first comprehensive studies exploring the impact of mass, metallicity, and rotation rates of WR stars’ on the ability to produce ionizing spectra hard enough to explain observed He II emission.

The remainder of this paper is as follows. In section 2, we describe our method for calculating expected nebular He II fluxes from stellar evolution and population synthesis models. In section 3, we present the results of our population synthesis modeling, focusing on the time evolution of ionizing photon luminosities and their ratios, and their dependence on various model parameters. We also analyze the nebular lines these photons drive, calculating intensity ratios and equivalent widths (EWs) of key emission lines so that we can compare our models to observations. We conclude the paper by summarising our findings and their implications in section 4.

## 2. Methods

Our objective is to obtain He<sup>+</sup> ionizing photon budgets produced by the single massive star channel, and then use these to compute nebular fluxes in the He II  $\lambda$ 4686 and He II  $\lambda$ 1640 emission lines. For this purpose we first produce a set of stellar tracks and atmospheres for single massive stars that have high  $T_{\text{eff}} \sim 80 - 100$  kK (subsection 2.1) and then process them through a stellar population synthesis code (subsection 2.2) to obtain the ionizing photon

budgets and spectra expected from stellar populations. Finally, we process the star cluster spectra through a photoionization code to derive the nebular spectra (subsection 2.3).

### 2.1. Stellar models

Massive stars on the main-sequence (MS) lose mass via high velocity ( $\sim \text{few} \times 1000$  km/s) and low mass-loading winds, with mass-loss rates  $\dot{M} \sim 10^{-6} M_\odot \text{ yr}^{-1}$ , yielding optically thin atmospheres. However, when these stars transition to the WR phase, in general during core He burning, their mass-loss rates typically increase by an order of magnitude to  $\dot{M} \sim 10^{-5} M_\odot \text{ yr}^{-1}$ , resulting in an extended optically thick atmosphere. Despite their high opacity, however, these atmospheres often exhibit clumpiness, which potentially allows ionizing photons to escape through the atmosphere and into the ISM through optically thin pathways. Our goal here is to parameterize this effect.

We begin from a set of stellar tracks, for which purpose we use MESA Isochrone Stellar Tracks (MIST; Choi et al. 2016) for two rotation rates,  $v/v_{\text{crit}} = 0.0, 0.4$  and for three metallicities,  $[\text{Fe}/\text{H}] = 0.0, -1.0, -2.0$  with a upper mass limit of  $150 M_\odot$ . At high masses the tracks have a mass interval  $\Delta M = 10 M_\odot$ , and we show in Appendix A that this relatively high resolution (compared to some other sets of tracks) is important to capture ionizing photon budgets accurately. For details of the MIST setup, such as adopted physical processes, parameter choices, etc., we refer the readers to Choi et al. (2016). These tracks yield, for each initial stellar mass, rotation rate, and metallicity, a set of stellar parameters as a function of time, the most important of which for what follows are the mass loss rate  $\dot{M}$ , stellar radius  $R$ , stellar luminosity  $L$ , and surface abundances of H, He, C, N, and O; we use these abundances to classify stars as either non-WR or WR, and within WR as one of several possible sub-types: WNL, WNE, WO, WC; see Choi et al. 2016 (who in turn take their scheme from Georgy et al. 2012) for full details of how the classification is performed. For further detailed discussions on WR subtypes, we refer the readers to Roy et al. 2020, 2021.

While we use the MIST tracks as a default because they are well-tested, they have a weakness that, like most stellar tracks, they assume that all elements follow Solar-scaled abundances. However, it is well established that at metallicities of 1/10th Solar and below this assumption is invalid; instead,  $\alpha$ -elements are enhanced due to the contributions from type-II supernovae without corresponding type-Ia events (Nicholls et al. (2017), and references therein). To ensure that our results do not depend on the assumption of Solar-scaled abundances, in Appendix B we repeat the analysis of the main text using the STROMLO STELLAR TRACKS (SST)<sup>1</sup> (Grasha et al. 2021), which use empirically-motivated “Galactic Concordance” abundances from Nicholls et al. rather than Solar-scaled abundances.

In order to predict the stellar spectrum at each point along an evolutionary track (see subsection 2.2), we require two more pieces of information: the effective temperature and radius of the stellar photosphere,  $T_{\text{eff}}$  and  $R_{\text{eff}}$ . For stars without optically thick winds, these are simple: the photosphere is at the stellar surface,  $R_{\text{eff}} = R$ , and the effective temperature is then given implicitly by the usual relation  $L = 4\pi R_{\text{eff}}^2 \sigma_{\text{SB}} T_{\text{eff}}^4$ . For WR stars with potentially opaque winds, however, the choice is much more subtle, because in such stars the photosphere could potentially be at a much larger radius than that from which the wind is launched, leading to a much lower effective temperature. We

<sup>1</sup> <https://sites.google.com/view/stromlotracks/home?authuser=0>

therefore consider three possible approaches to calculating  $R_{\text{eff}}$  and  $T_{\text{eff}}$  for WR stars.

### 2.1.1. Highly-clumped and porous winds

One option is to assume that the wind is sufficiently clumped and porous that the solid angle over which it is optically thick covers only a minority of the stellar surface, in which case the effects of the wind are small and we can set  $R_{\text{eff}}$  and  $T_{\text{eff}}$  for WR stars exactly as for all other stars. This is the limit of close to optically thin winds, and is the default option for the MIST tracks, i.e., the values of  $R_{\text{eff}}$  and  $T_{\text{eff}}$  reported by Choi et al. (2016) are computed in this way.

### 2.1.2. Spherically homogeneous laminar winds

A second possibility is to treat the wind as spherical and homogenous, and compute the location of the photosphere under this assumption. As a proxy for the cooler temperatures resulting from these extended atmospheres of stars with strong mass loss, we adopt the prescription of Schaller et al. (1992), which we briefly summarise here for readers' convenience. This scheme assumes the wind follows the standard velocity law

$$v(r) = v_{\infty} \left(1 - \frac{R}{r}\right)^{\beta}, \quad (1)$$

where  $v(r)$  is the radial velocity,  $\beta$  is the acceleration index for the wind, and  $v_{\infty}$  and  $R_{\text{eff}}$  are the terminal velocity and stellar radius, respectively. Following Pauldrach et al. (1986), we adopt  $\beta = 2$  and  $v_{\infty} = 2 \times 10^3 \text{ km s}^{-1}$ . To compute the optical depth through this wind, we note that the flux-weighted mean opacity can be written as

$$\bar{\kappa} = \sigma_e [1 + M], \quad (2)$$

where  $\sigma_e$  is the opacity for electron scattering and  $M$  is the force-multiplier denoting the radiative acceleration due to lines in units of  $g_{\text{Eddington}}$  ( $= \kappa L / 4\pi c r^2$ , where  $c$  is the speed of light, and  $\kappa$  is the wind opacity).  $\sigma_e$  can be written as (equation 8.93 of Lamers & Cassinelli (1999)),

$$\sigma_e = \frac{\sigma_T n_e}{\rho} = 0.401 \left( I_{\text{H}} X + I_{\text{He}} \frac{Y}{4} + I_{\text{Z}} \frac{Z}{14} \right) \text{ cm}^2 \text{ g}^{-1}, \quad (3)$$

where  $\sigma_T = 6.6524 \times 10^{-25} \text{ cm}^2$  is the Thomson scattering cross-section of electrons,  $\rho$  is the total mass density,  $n_e$  is the electron density,  $I_{\text{H}} = 1$ ,  $I_{\text{He}} = 2$  and  $I_{\text{Z}} = 14$  are the number of electrons per ion of H, He and heavier elements, respectively, and  $X$ ,  $Y$ , and  $Z = 1 - X - Y$  are the mass-fractions of H, He, and heavier atoms at the stellar surface (which we know from the stellar tracks). The optical depth, therefore, in terms of  $\bar{\kappa}$ , is

$$\tau(r) = \int_r^{\infty} \bar{\kappa} \rho \, dr = \int_r^{\infty} \sigma_e \rho \, dr + \int_r^{\infty} \sigma_e M \rho \, dr = \tau_e + \tau_{\text{lines}}, \quad (4)$$

where

$$\tau_e = \frac{\sigma_e \dot{M}}{4\pi v_{\infty} (1 - \beta) R} \left[ 1 - \frac{1}{(1 - R/r)^{\beta-1}} \right], \quad (5)$$

is the electron scattering optical depth and  $\rho = \dot{M} / 4\pi r^2 v(r)$  is the mass density in the wind for a star with mass loss rate  $\dot{M}$ . We

calculate  $\tau_{\text{lines}}$  from the prescription of Kudritzki et al. (1989) for the force-multiplier  $M$  as

$$M \left( \rho, r, v, \frac{dv}{dr}, n_e \right) = k \left( \frac{\sigma_e \rho v_{\text{th}}}{dv/dr} \right)^{-\alpha} \left( \frac{n_e}{W(r)} \right)^{\delta} \text{CF} \left( r, v, \frac{dv}{dr} \right), \quad (6)$$

where  $v_{\text{th}} = \sqrt{2k_{\text{B}}T_{\text{eff}}/m_{\text{H}}}$  is the thermal velocity of protons,  $k_{\text{B}}$  and  $m_{\text{H}}$  are the Boltzmann constant and proton mass respectively,  $W$  and  $\text{CF}$  are the dilution and correction factors respectively coming from the non-radial streaming of photons, and  $k$ ,  $\alpha$ , and  $\delta$  are numerical fitting factors that are obtained by comparing the analytic prescription above to numerical results; Kudritzki et al. follow Pauldrach et al. (1986) in setting  $k = 0.124$ ,  $\alpha = 0.64$ , and  $\delta = 0.07$ , and we do the same. We then compute  $n_e/W(r)$  as (Kudritzki et al. 1989, equation 42)

$$\left( \frac{n_e}{W(r)} \right)^{\delta} = \Delta 2^{\delta} \left[ q(\delta, \beta) \left( \frac{R}{r} \right)^2 + 1 \right] \quad (7)$$

$$\Delta = \left( \frac{\dot{M}}{4\pi R^2 v_{\infty}} \frac{2}{m_{\text{H}}} \frac{1 + I_{\text{He}} Y}{1 + 4Y} \times 10^{-11} \text{ cm}^3 \right)^{\delta}, \quad (8)$$

and the numerical factor  $q(\delta, \beta) = 0.244$  for our chosen values of  $\delta$  and  $\beta$ . Similarly, we compute  $\text{CF}$  as (Kudritzki et al. 1989, equation 15),

$$\text{CF} = \frac{1}{\alpha + 1} \frac{x^2}{1 - h(x, \beta)} \left[ 1 - \left( 1 - \frac{1}{x^2} + h(x, \beta) \frac{1}{x^2} \right)^{\alpha+1} \right], \quad (9)$$

where  $x \equiv r/R$  and  $h(x, \beta) \equiv (x - 1)/\beta$ .

The expressions above fully specify the force multiplier  $M$  at each radius, and therefore put us in a position to compute  $\tau(r)$  for arbitrary  $r$  by evaluating the integrals in Equation 4. We can in turn then find the radius  $r$  for which  $\tau(r) = 2/3$ , which defines our effective radius  $R_{\text{eff}}$  and implicitly our effective temperature  $T_{\text{eff}}$ . We carry out this calculation for every point in our stellar evolution calculation where stars are classified as WR.

### 2.1.3. Partially-clumped winds

The previous two schemes represent the limits of very strongly clumped and porous winds and completely laminar winds, but we can also consider an intermediate case motivated by the results of three-dimensional simulations. Moens et al. (2022) performed the first ever time-dependent 3D radiation-hydrodynamical simulations of WR star winds, and tabulate the effective temperatures of the resulting structures (their Table 2). Comparing their results for a high-luminosity  $10 M_{\odot}$  star with a clumping factor<sup>2</sup> of  $\approx 2$  to the  $T_{\text{eff}}$  we compute for a star of comparable mass and luminosity using the laminar wind prescription described in subsection 2.1.2, we find that the 3D simulation yields a factor of  $\approx 2$  larger  $T_{\text{eff}}$ . As a crude estimate of the effects of partial clumping, we therefore take  $T_{\text{eff}}$  for this case to be twice the value returned using the spherical wind prescription from subsection 2.1.2. We note that this is a conservative lower limit for the effects of partial clumping, since  $10 M_{\odot}$  is at the low mass end for WR stars and 2 is a relatively low clumping factor, and we expect the difference between the laminar and clumped value of  $T_{\text{eff}}$  to be larger for higher stellar masses and wind clumping factors.

<sup>2</sup> Typically the extent of clumping is defined by the clumping factor,  $D_{\infty} = \langle \rho^2 \rangle / \langle \rho \rangle^2$ , where  $\langle \rho \rangle$  is the mean density of the atmosphere.

We caution that this approximation is rather crude, since in reality if the wind has partial coverage of the stellar surface then a better description than a single intermediate effective temperature might be a weighted sum of the outputs of atmospheres with two different effective temperatures and surface gravities – one representing the contribution from parts of the stellar surface that are directly visible from infinity and one representing areas where the wind is opaque enough to obscure the surface and the photosphere forms much further out. Given the hugely non-linear dependence of hard ionizing photon production on  $T_{\text{eff}}$  (as we shall see below), the results from such a mixing model might be quite different from the results we obtain here by specifying a single, intermediate  $T_{\text{eff}}$ . However, the development of such improved models for wind partial covering is beyond the scope of this paper, and we therefore resort to the single  $T_{\text{eff}}$  approximation, keeping in mind that, even if this approximation is of limited accuracy, the results of partial clumping should nonetheless be bounded between the highly-clumped and laminar cases we have defined above.

## 2.2. Population synthesis modelling

Having obtained values for  $R_{\text{eff}}$  and  $T_{\text{eff}}$  at each point in the stellar tracks via the three possible methods described above, we next generate synthetic spectra for stellar populations by using these stellar tracks in the Stochastically Lighting Up Galaxies (SLUG<sup>3</sup>) code (da Silva et al. 2012; Krumholz et al. 2015). We compute spectra for star clusters with ages from 0.1 – 10 Myr with a time step of 0.1 Myr. Given that the observed clusters that produce He II emission are likely substantially more massive than  $\sim 10^3 - 10^4 M_{\odot}$ , the range below which stochastic sampling generally becomes important, we turn off SLUG’s stochastic features and treat the IMF as fully sampled; for this mode the total cluster mass simply acts as a multiplicative constant on the output spectrum. We assume a Chabrier IMF (Chabrier 2003). We generate spectra using SLUG’s “starburst99” model for stellar atmospheres, which replicates the model used in starburst99 (Leitherer et al. 1999; Vázquez & Leitherer 2005). This model uses a library of Kurucz model atmospheres taken from Lejeune et al. (1997) for stars without strong winds, models from Pauldrach et al. (2001) for OB stars with optically thin winds, and models from Hillier & Miller (1998) for WR stars.

## 2.3. Nebular modelling: spectral synthesis models

To generate nebular spectra, we use the spectra produced by SLUG as inputs to a calculation of the structure and emission from a photoionized nebula using CLOUDY<sup>4</sup> (Chatzikos et al. 2023). To perform these calculations we normalize the total luminosity of the stellar population to that of a cluster of mass  $10^6 M_{\odot}$ , and place an innermost zone for the nebula at a distance of 1 pc from this population. We then use CLOUDY to calculate a hydrostatic structure for the resulting nebula, adopting CLOUDY’s “expanding sphere” prescription for H II region geometry and setting the nebula to be isobaric at a pressure  $\log(P/k_B [\text{K cm}^{-3}]) = 7$ . We choose our mass normalization and pressure to be typical of values inferred for observed He II-emitting regions, but we have verified that varying these choices over plausible ranges leads to negligible differences in the qualitative results for the line ratios in

which we are interested below.<sup>5</sup> We set the abundances of the 30 non-hydrogenic elements included in CLOUDY to values consistent with those assumed in the MIST models from which we generate the stellar tracks; this means that nebular abundances properly scale with stellar ones. We further adopt CLOUDY’s default grain composition for H II regions of Solar metallicity, scaling the total grain abundance by factors of 0.1 and 0.001 for  $[\text{Fe}/\text{H}] = -1$  and  $-2$  respectively, following Rémy-Ruyer et al. (2014)’s findings with regard to variation of the dust-to-gas ratio with metallicity (see the discussion of Figure 4 of Rémy-Ruyer et al. 2014). We stop running the models when either the electron temperature falls below 1000 K or the electron fraction, defined as the ratio of electron to total hydrogen densities, falls below 0.1. In addition to stellar radiation, we also include CLOUDY’s default cosmic ray background.

## 3. Results

Here we describe the results of our nebular He II modelling. We start in subsection 3.1 by examining ionizing photon budgets and their dependence on model parameters, most importantly on our adopted treatment of stellar wind clumping. In subsection 3.2 we analyze synthetic spectra of H II regions, testing under what circumstances our models can reproduce key features of observed He II emitters such as He II to H $\beta$  intensity ratios and the equivalent widths of prominent lines such as H $\beta$ , He II, and the blue bump lines.

### 3.1. Ionizing photon budgets

In this section, we quantify how these various choices in our treatment of stellar evolution and atmosphere modelling affect ionizing photon budgets.

#### 3.1.1. Extended atmosphere correction

We start our inspection with the most crucial yet most uncertain parameter: the scheme used to model clumpy WR atmospheres, as described in subsection 2.1. In Figure 1 we show the time evolution of the instantaneous H I-, He I-, He II-ionizing photon luminosities (left), along with the cumulative output in these three bands (right), for our three wind opacity schemes: spherically homogeneous optically thick winds, partially clumpy, and very clumpy and porous (close to optically thin winds). This plot is for the case  $[\text{Fe}/\text{H}] = 0.0$ ,  $v/v_{\text{crit}} = 0.0$  and for a cluster mass of  $M_{\text{cl}} = 10^6 M_{\odot}$ ; we explore the effects of sub-solar metallicity and rotation below. We find that H I photon luminosities have similar values irrespective of wind opacities, with the homogeneous and highly clumpy winds’ results differing by only  $\sim 3\%$  once they reach the asymptotic plateau at  $\gtrsim 5$  Myr. The differences are much larger for harder photons: cumulative photon output differs by  $\sim 17\%$  for He I, and  $\sim 2000\%$  (a factor of 20) for He II.

The difference between the models is almost entirely due to the rate of hard ionizing photon production at times from

<sup>5</sup> The sole exception to this statement is for the case of a stellar population with  $v/v_{\text{crit}} = 0.0$ ,  $[\text{Fe}/\text{H}] = -1$  for the highly clumped and porous winds at 5 Myr, for which at the chosen pressure and luminosity the system admits two distinct solutions for the structure of the nebula, one lower temperature and higher density and one lower density and higher temperature, with somewhat different line ratios; changing the cluster mass or pressure can then cause one of the two solution branches to disappear. However, since this is only one case out of a large number of models, we will not worry about this complication further.

<sup>3</sup> <https://bitbucket.org/krumholz/slug2/src/master/>

<sup>4</sup> <https://gitlab.nublado.org/cloudy/cloudy>

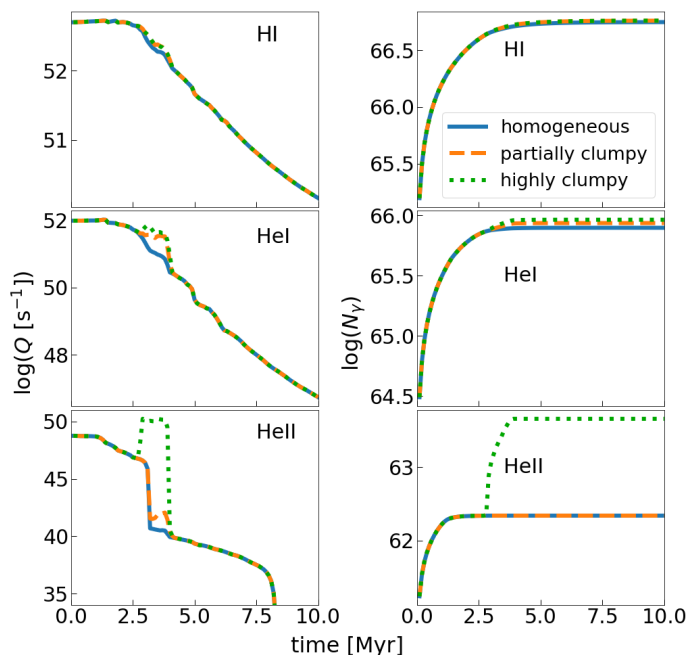


**Fig. 1.** *Left:* Time evolution of H I, He I, He II photon luminosities  $Q(t)$  (number of photons emitted per unit time) for the three wind prescriptions: optically thick and homogeneous winds, partially clumpy, and highly-clumped close to optically thin winds. The results shown are for non-rotating Solar metallicity stars and for a star-cluster mass of  $10^6 M_\odot$ . *Right:* Cumulative photon emission,  $N_\gamma = \int_0^T Q(t) dt$ , as a function of time  $T$  for the same parameters.

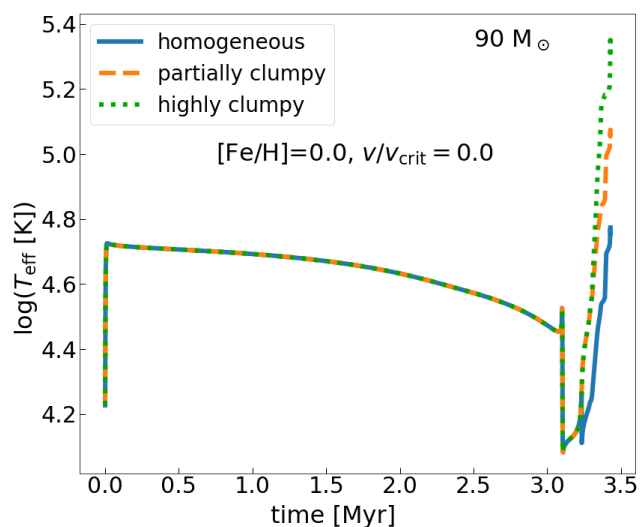


**Fig. 2.**  $T_{\text{eff}}$  versus time for  $90 M_\odot$  stars with  $[\text{Fe}/\text{H}] = 0.0$  and  $v/v_{\text{crit}} = 0.0$ , with WR winds modelled with three different atmosphere morphologies.

$\approx 2.5 - 4$  Myr, when stars  $\geq 70 M_\odot$  enter their WR phases. To understand the origin of this difference in more detail, we focus on one example case: a non-rotating, Solar metallicity star with an initial mass of  $90 M_\odot$ . We examine the time evolution of  $T_{\text{eff}}$  for this star in Figure 2, which shows that the optically thick atmosphere reaches a maximum temperature of  $\log(T_{\text{eff}}) \approx 4.8$  during the WR phase, too cool to produce significant quantities of harder photons capable of ionizing He II and with limited production of He I-ionizing photons. In contrast, the partially clumpy

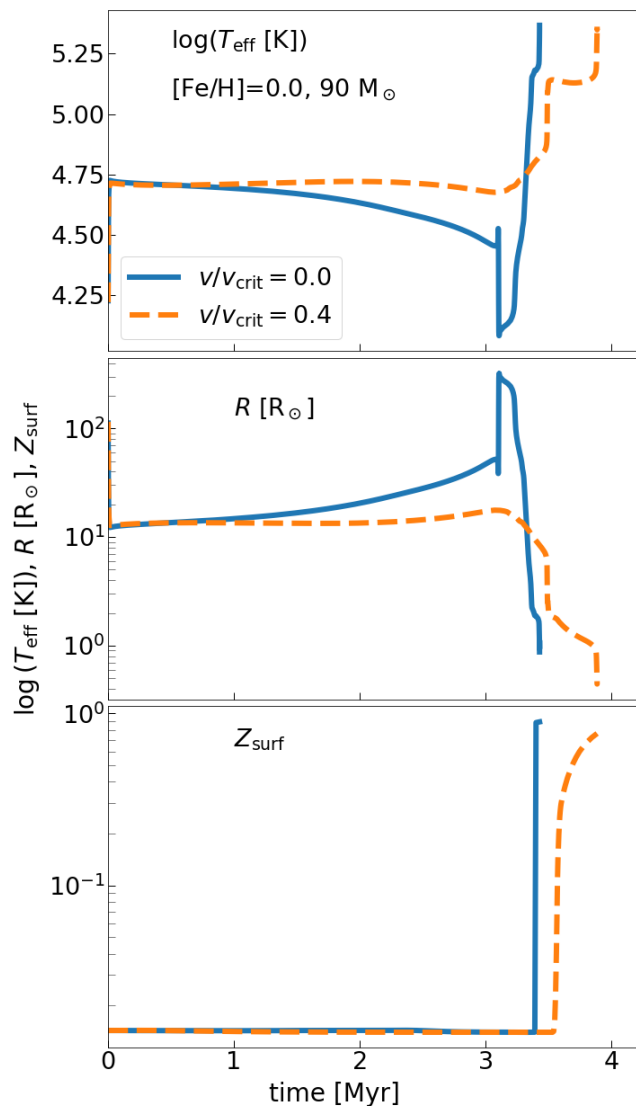


**Fig. 3.** Time evolution of  $\log(T_{\text{eff}})$  (top panel),  $R$  (middle), and surface metal abundance  $Z_{\text{surf}}$  (bottom) for  $90 M_\odot$  solar-metallicity stars rotating at  $v/v_{\text{crit}} = 0.0$  and  $0.4$ . We measure these parameters at the surface of the hydrostatic core because we calculate them for the spherically homogeneous, laminar winds.

wind achieves a temperature as high as  $\log(T_{\text{eff}}) = 5.0$ , but not higher, leading to the substantial production of He I photons, but still few harder photons past the He II ionization edge. For the highly-clumped, close to optically thin atmosphere, the surface temperature reaches  $\log(T_{\text{eff}}) \geq 5.2$  at  $\geq 3$  Myr, resulting in the significant production of photons capable of ionizing both He I and He II. Given this large difference, for the remainder of this paper we focus on highly-clumped winds as our fiducial case unless explicitly stated otherwise, with the intention of exploring the maximum He II ionizing photon budgets and the corresponding line intensities achievable via single WR-star pathways.

### 3.1.2. Rotation

Now that we have established that our models can in some cases produce large quantities of He II-ionizing photons when the winds are highly-clumped, we next examine the importance of stellar

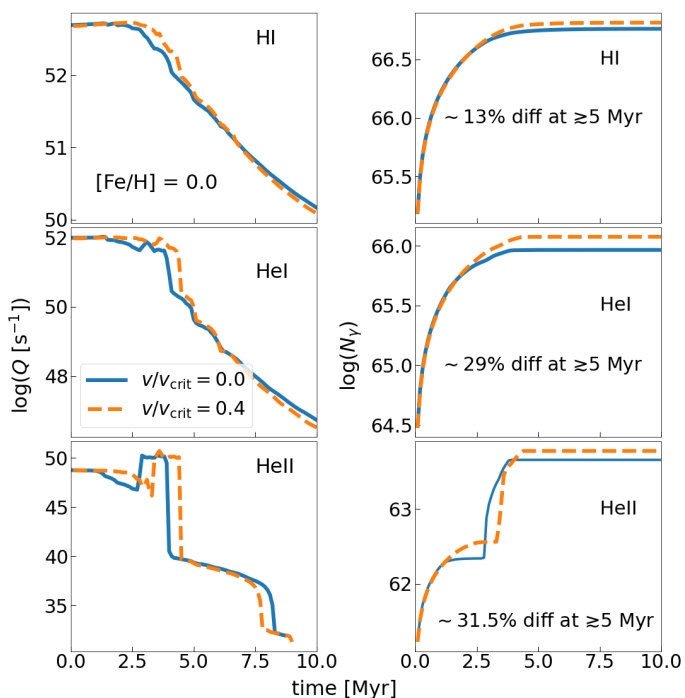


**Fig. 4.** Same as Figure 1, but now showing the results for highly clumped and porous winds for two different rotation rates  $v/v_{\text{crit}} = 0.0$  and  $0.4$ .

rotation. From the standpoint of production of hard ionizing photons, rotation has two major effects:

- **Longer MS and WR lifetime:** Rotation enhances the mixing of chemical elements in a massive star, leading to Chemically Homogeneous Evolution (CHE) in the most extreme cases for stars  $\geq 90 M_{\odot}$ . This increased mixing extends the supply of hydrogen fuel to the core, prolonging the star’s MS lifetime. However, following the typical definition of WR stars, having high  $T_{\text{eff}}$  ( $\geq 10^4$  K) and high helium mass-fraction ( $\geq 40\%$ ), rotating stars with masses  $\geq 70 M_{\odot}$  enter the WR phase when they are still on the MS (core H burning). Moreover, the WR lifetime also enhances for rotating stars because the helium fuel supply to the core lasts longer in the most extreme cases for stars  $\geq 90 M_{\odot}$ , similar to the extended hydrogen fuel supply during the MS. Thus, the combined effect of the early entry to the WR phase and the prolonged lifetime makes the rotating star to spend a longer duration in the WR phase.
- **Enhanced surface opacity:** Rotation may enhance the heavy element abundances at the surface of WR stars, and hence in the winds, through two channels. First, rotation directly enhances the mass-loss rate in the MIST framework following the prescription  $\dot{M}(v) = \dot{M}(0) (1/(1 - v/v_{\text{crit}}))^{\zeta}$ , where  $\dot{M}(v)$  is the mass loss rate as a function of rotation velocity  $v$ , and  $\zeta$  is set to 0.43 based on numerical calibrations (Friend & Abbott 1986; Langer 1998); see Section 3.7.3 of Choi et al. (2016) for details. Second, rotation-induced instabilities bring heavy elements from the core to the stellar surface, and this combined with rotation-enhanced mass loss exposing deeper layers in the star yields a significant enhancement in the abundance of heavy elements at the stellar surface (Roy et al. 2020). Both the higher mass loss and the larger heavy element abundances increase the wind opacity.

To explore the effect of rotation, in Figure 3 we show the time evolution of  $T_{\text{eff}}$ , radius, and the surface metallicity  $Z_{\text{surf}}$

(defined as the mass fraction in elements heavier than He) for the same  $90 M_{\odot}$ , Solar-metallicity case shown in Figure 2, but now comparing the cases  $v/v_{\text{crit}} = 0.0$  and  $0.4$ ; the former is the same as the highly clumpy winds shown in Figure 2. We find that the non-rotating star inflates towards the end of the MS, resulting in decreased  $T_{\text{eff}}$ . Subsequently, it begins losing mass rapidly due to the combination of low surface gravity and high mass ( $\geq 80 M_{\odot}$ ) and thus luminosity. As a result, the star shrinks, exposing the “fossil” convective core and producing high surface metal abundance and  $T_{\text{eff}}$  soon after the star enters the WR phase. However, this phase is short-lived ( $\sim 0.2$  Myr). In contrast, the rotating star spends a longer duration in the WR phase because of the early entry into this phase. As the star enters the WR phase, both  $T_{\text{eff}}$  and  $Z_{\text{surf}}$  increase significantly, while the radius slowly decreases.

Having understood the evolution of a single massive star at two different rotation rates, we now return to the broader question of how rotation affects IMF-averaged hard photon production. In Figure 4, we plot the ionizing photon budgets for  $10^6 M_{\odot}$ , Solar-metallicity clusters with highly-clumped winds at  $v/v_{\text{crit}} = 0$  and  $0.4$ ; the  $v/v_{\text{crit}} = 0$  case shown in this Figure is identical to the highly-clumped winds shown in Figure 1. We see that the longer duration spent as a WR star in the rotating case leads to higher budgets of H I-, He I-, and He II-ionizing photons. Consistent with what we found when examining treatments of clumping, sensitivity is greatest for the highest-energy photons: we find differences of  $\sim 15\%$ ,  $\sim 30\%$  and  $\sim 32\%$  for the cumulative budgets of H I, He I, and He II, respectively, at  $\geq 5$  Myr. However, recall that changing the clumping factor produced a factor of  $\approx 20$  change in the He II-ionizing photon budget; in comparison, we see that the effects of rotation are substantially smaller.

### 3.1.3. Metallicity

We next examine the effect of the initial stellar metallicity, which also affects hard ionizing photon production. Surface metallicity is a determining factor for mass loss, with higher metallicities resulting in higher loss rates due to stronger line-driven winds<sup>6</sup>. More metal-rich stars therefore have larger mass loss rates prior to the WR phase, and this higher envelope loss in turn makes it easier to expose stars’ “fossil”-convective cores (cores that are no longer convective, but were part of the convective cores in the previous evolutionary stages; for details see Roy et al. (2020)), which are heavily helium-enhanced due to CNO burning. This leads to the earlier entry into the WR phase.

In Figure 6 we show the metallicity dependence through the time evolution of  $T_{\text{eff}}$  (top panels), radius (middle) and surface  $Z_{\text{surf}}$  (bottom panels), again focusing on the example of a  $90 M_{\odot}$  star; we show both the non-rotating (left panels) and rotating,  $v/v_{\text{crit}} = 0.4$  (right panels) cases. For non-rotating stars, we observe that as  $[\text{Fe}/\text{H}]$  decreases, the main-sequence (MS) lifetime increases significantly:  $\sim 3.3$  Myr for Solar metallicity versus  $\sim 3.7$  Myr for  $[\text{Fe}/\text{H}] = -1.0$ . This is because at low metallicity, the initial hydrogen mass fraction is larger compared to the metal-rich star, and also the convective core mass increases as the metallicity decreases; the combined effect of which enhances the hydrogen fuel reservoir for the metal-poor star enhancing its MS lifetime. As we approach the WR phase, the stronger mass loss in

<sup>6</sup> Note that metal line-driven mass-loss rates are actually dependent on the iron surface abundances, not on the total surface metallicity (Sander et al. (2020) and references therein). However, our MIST models account for the surface metallicity, in order to keep it similar to the other existing 1D stellar evolution codes (for example, the **GENEVA STELLAR TRACKS**).

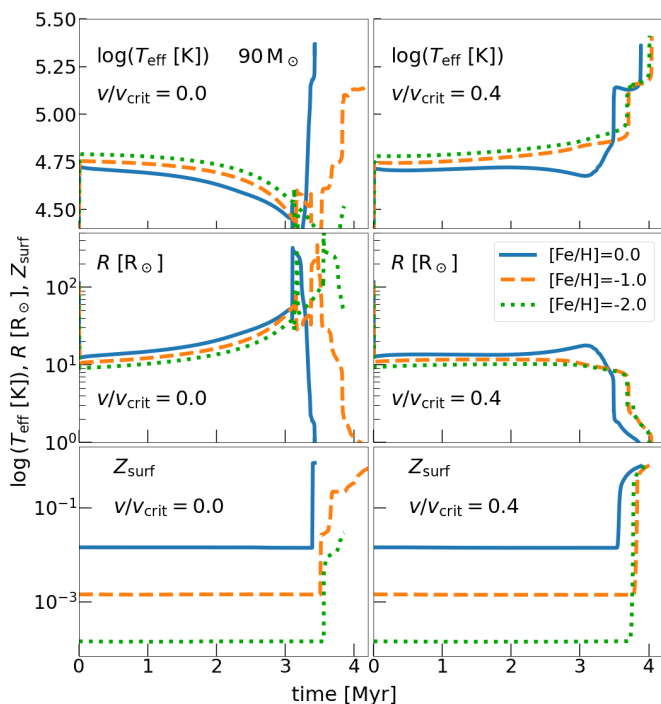


**Fig. 5.** Same as Figure 3, but now showing the result for three different initial metallicities:  $[\text{Fe}/\text{H}] = 0.0$  (blue solid lines),  $-1.0$  (orange dashed lines), and  $-2.0$  (green dotted lines). The left panels correspond to  $v/v_{\text{crit}} = 0.0$  and the right panels show  $v/v_{\text{crit}} = 0.4$ .

the two more metal-rich cases ( $[\text{Fe}/\text{H}] = 0.0$  and  $-1.0$ ) causes the stars to shrink rapidly and expose their metal-rich fossil convective cores, producing a sudden increase in  $T_{\text{eff}}$  and surface metallicity; this effect is greatly diminished for  $[\text{Fe}/\text{H}] = -2.0$ . In contrast, with rotation (right panels), the surface parameters become nearly independent of metallicity because rotation induced mixing leads to CHE for stars  $\geq 90 M_{\odot}$  bringing helium from the core to the surface, that allow stars to enter the WR phase even with lower mass losses. Consequently, the MS lifetimes are only weakly dependent on  $[\text{Fe}/\text{H}]$ , with only about a 3% difference between Solar and 1/10th Solar metallicity, and less than 1% difference between  $[\text{Fe}/\text{H}] = -1.0$  and  $-2.0$ .

We show how these changes affect the IMF-averaged ionizing photon budgets in Figure 6 and Figure 7 for the non-rotating and rotating cases, respectively. We find that for softer ionizing photons (H I, He I) in non-rotating stars, the ionizing luminosity increases monotonically as  $[\text{Fe}/\text{H}]$  decreases due to decreasing surface opacity, and thus decreasing wind opacity, and increasing surface temperature. For He II, on other hand, we find that ionizing photon output is maximized at  $[\text{Fe}/\text{H}] = -1.0$ , and is lower at both  $-2.0$  and  $0$ . This pattern holds true only for non-rotating stars. We can understand this non-monotonic behavior as a result of a competition between two effects. One is the same mechanism we have already invoked to explain the softer photons: as we lower the metallicity we lower the opacity, raising the surface temperature and increasing the escape of ionizing radiation. The other competing effect is mass loss: stars lose more mass at higher metallicity, which in turn means that once stars enter the WR phase, they have smaller radii and higher effective temperatures, favoring production of harder ionizing photons as the metallicity increases. The competition between these effects yields a maximum for He II ionizing photon production at  $[\text{Fe}/\text{H}] = -1.0$ . The effect has importance only for the non-rotating case because

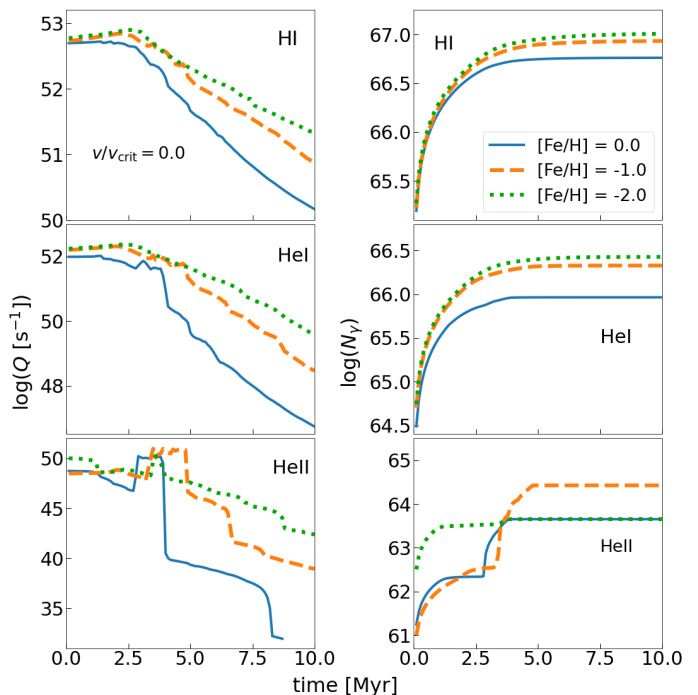


**Fig. 6.** Same as Figure 1, but now showing the results for three different metallicities,  $[\text{Fe}/\text{H}] = 0.0$ ,  $-1.0$ , and  $-2.0$ , for non-rotating stars. The  $[\text{Fe}/\text{H}] = 0.0$  case shown here is identical to the highly-clumped winds shown in Figure 1.

this is the case for which the initial surface metallicity has the impact on stellar mass-loss. For this case,  $[\text{Fe}/\text{H}] = -1.0$  yields a cumulative He II-ionizing photon production that is a factor of  $\approx 5$  larger than either the metallicity 0 or  $-2$ .

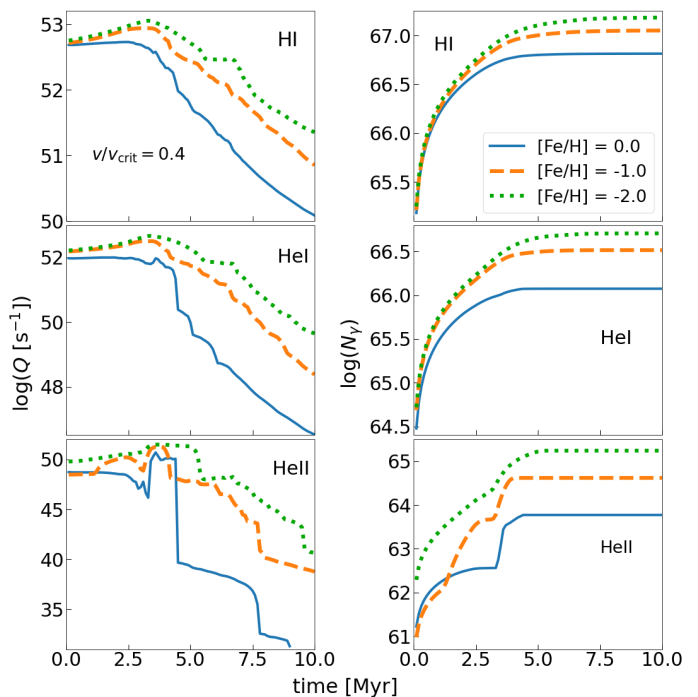


**Fig. 7.** Same as Figure 6, except for now the stars are rotating at  $v/v_{\text{crit}} = 0.4$ .



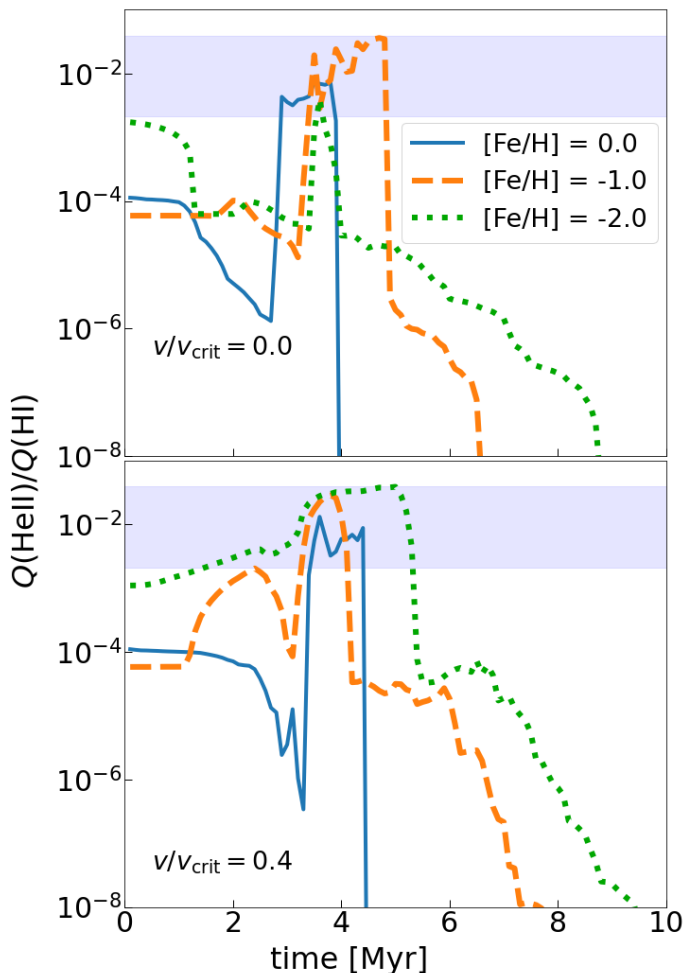


**Fig. 8.** Time evolution of  $Q(\text{He II})/Q(\text{H I})$  for non-rotating (top panel) and rotating stars with  $v/v_{\text{crit}} = 0.4$  (bottom panel) for three metallicities  $[\text{Fe}/\text{H}] = 0.0$  (blue solid line),  $-1.0$  (orange dashed),  $-2.0$  (green dotted), and for highly-clumped winds. The blue band shows the approximate range of  $Q(\text{He II})/Q(\text{H I}) \sim 0.0021 - 0.0371$  expected to produce line intensity ratios  $I(\text{He II } \lambda 4686)/I(\text{H}\beta)$  in the range observed in spatially-resolved observations of the Cartwheel Galaxy (Mayya et al. 2023),  $\approx 0.004 - 0.07$ .

On the contrary, in rapidly rotating stars, CHE for the most massive stars  $\geq 90 M_{\odot}$  facilitates the early entry to the WR phase prolonging the WR lifetime, even at low metallicities, despite reduced metal line-driven mass loss, resulting in nearly uniform surface abundances across different metallicities. Consequently, there is a monotonicity in the increment in ionizing luminosity as  $[\text{Fe}/\text{H}]$  decreases for both softer and harder ionizing photons. We find that for this case with  $v/v_{\text{crit}} = 0.4$ ,  $[\text{Fe}/\text{H}] = -2.0$  yields a cumulative He II-ionizing photon budget that is a factor of  $\approx 29$  and  $\approx 4$  larger than that of solar metallicity and  $-1$ , respectively.

Thus, to conclude, rotating stars with  $v/v_{\text{crit}} \geq 0.4$  provides a more favourable scenario for the He II ionizing photon production across all metallicities.

### 3.1.4. From ionizing photon budgets to line ratios

Having discussed the dependence of various stellar parameters on the ionizing photon budgets, we are now in a position to address the central, motivating question for this study: under what cir-

cumstances can stars with clumpy winds drive the bright nebular He II lines seen in some star-forming galaxies? In subsection 3.2 we will carry out full nebular photoionisation calculations.

Our simple approximation is to treat emission in both the He II  $\lambda 4686$  and  $\text{H}\beta$  lines as arising purely from recombinations occurring in a uniform-temperature, dust-free, photon-bounded H II region within which all photons above the He II ionization threshold are absorbed by He<sup>+</sup> ions and all photons below that energy but above 1 Ryd are absorbed by neutral H. Since the number of photons above the He II threshold is small compared to the total ionizing flux, in this case we can simply equate the H I-ionizing flux with the rate of recombinations to H I, with a fixed fraction of those recombinations yielding emission of a photon in the  $\text{H}\beta$  line, and we obtain the usual relation between ionizing photon emission and  $\text{H}\beta$  line luminosity:

$$L(\text{H}\beta) = E_{\text{H}\beta} \alpha_B(\text{H}\beta, T) Q(\text{H I}) \approx 1.94 \times 10^{-13} Q(\text{H I}) \text{ erg} \quad (10)$$

where  $\alpha_B(\text{H}\beta, T)$  is the effective recombination coefficient for  $\text{H}\beta$  emission in case B as a function of the temperature  $T$ , and our numerical evaluation is appropriate for  $T \approx 10^4$  K. Similarly, we can equate the recombination rate to He II with the production rate of He II-ionizing photons, and compute the luminosity of the He II  $\lambda 4686$  line as (Kehrig et al. 2015)

$$L(\text{He II}) = E_{\text{He II}} \alpha_B(\text{He II}, T) Q(\text{H I}) \approx 3.66 \times 10^{-13} Q(\text{He II}) \text{ erg}, \quad (11)$$

where  $E_{\text{He II}}$  and  $\alpha_B(\text{He II}, T)$  are the He II  $\lambda 4686$  photon energy and recombination rate coefficient. Combining these results, we find that under our simple approximations the intensity ratio for the He II  $\lambda 4686$  and  $\text{H}\beta$  lines should be related to the emission rates of H I- and He II-ionizing photons by

$$\frac{I(\text{He II})}{I(\text{H}\beta)} = 1.89 \frac{Q(\text{He II})}{Q(\text{H I})}. \quad (12)$$

Kehrig et al. (2015) show that varying the temperature leads to only small variations in this ratio.

Since typical observed  $I(\text{He II})/I(\text{H}\beta)$  ratios in He II-emitting nebulae such as those found in the Cartwheel Galaxy are  $\sim 0.004 - 0.07$  (Mayya et al. 2023), this simple analysis suggests that stellar populations that produce ionizing photon ratios  $Q(\text{He II})/Q(\text{H I}) \sim 0.0021 - 0.0371$  will provide a reasonable match to observations. To see how our models compare to this range, in Figure 8 we show the time evolution of  $Q(\text{He II})/Q(\text{H I})$  for two rotation rates  $v/v_{\text{crit}} = 0.0$  (top panel) and  $0.4$  (bottom panel), and three metallicities  $[\text{Fe}/\text{H}] = 0.0$ ,  $-1.0$ , and  $-2.0$  (blue solid, orange dashed, and green dotted lines respectively), again focusing in the case of highly-clumped winds. We indicate our target range of  $Q(\text{He II})/Q(\text{H I})$  by the blue band. We see that all three metallicities can produce ratio in this range during the period immediately after the most massive stars enter the WR phase at  $\sim 3$  Myr, regardless of rotation rate. However, for non-rotating stars, only the two higher-metallicity cases remain in this range for  $\approx 1 - 1.5$  Myr, while the lowest metallicity case enters the range only briefly. On the other hand, for the rotating case, all three metallicities remain in this range for  $\sim 1.5 - 2.5$  Myr. Nonetheless, Figure 8 clearly demonstrates that populations of single massive stars with very clumpy atmospheres can produce  $Q(\text{He II})/Q(\text{H I})$  ratios that are in principle high enough to reproduce the  $I(\text{He II})/I(\text{H}\beta)$  ratios found in He II-emitting nebulae.

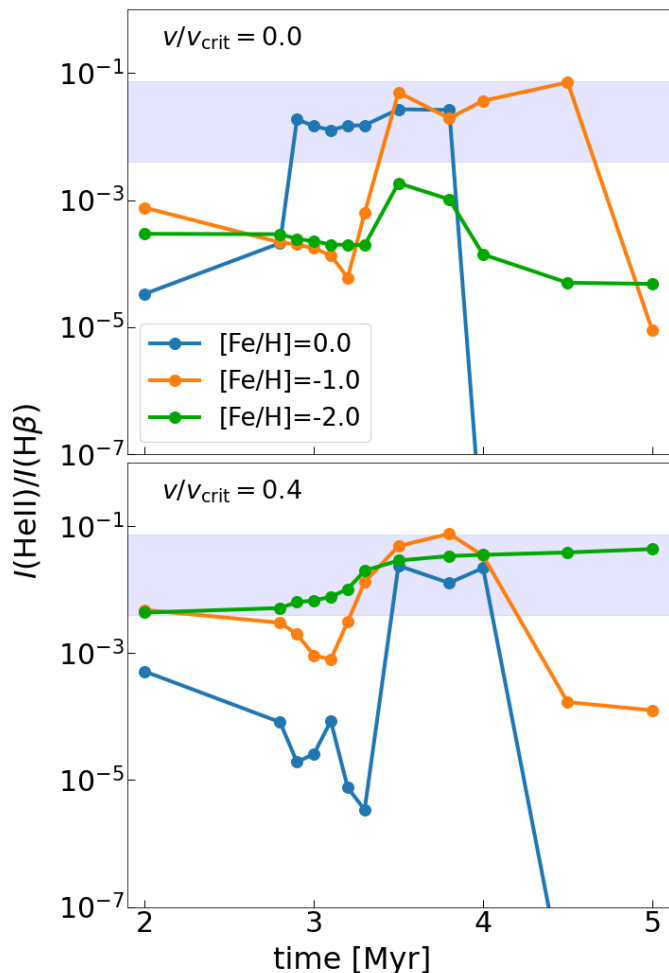


**Fig. 9.** Time evolution of  $I(\text{He II})/I(\text{H}\beta)$  for stellar populations with highly clumped winds at three metallicities,  $[\text{Fe}/\text{H}] = 0.0$  (blue),  $-1.0$  (orange), and  $-2.0$  (green), and two rotation rates  $v/v_{\text{crit}} = 0.0$  (top panel) and  $0.4$  (bottom panel).

### 3.2. Nebular spectral synthesis

While subsection 3.1.4 is suggestive, our calculations with `CLOUDY`, as detailed in subsection 2.3, provide more realistic results that include all the complexity we neglected in our simple analytic approximation. They also enable us to examine other observables such as the equivalent widths of the He II and blue bump lines. To this end, we generate synthetic nebular spectra using the procedure outlined in subsection 2.3 at stellar population ages of 2.0, 2.8, 2.9, 3.0, 3.1, 3.2, 3.3, 3.5, 3.8, 4.0, 4.5, and 5.0 Myr; these times provide good coverage of the range of times over which Figure 8 suggests that stellar populations are in the right range of ionizing photon ratio to produce line emission consistent with observations.

#### 3.2.1. $I(\text{He II})/I(\text{H}\beta)$

In Figure 9 we show the time evolution of the line intensity ratio  $I(\text{He II})/I(\text{H}\beta)$  for three metallicities,  $[\text{Fe}/\text{H}] = 0.0$  (blue),  $-1.0$  (orange), and  $-2.0$  (green), and two rotation rates,  $v/v_{\text{crit}} = 0.0$  (the top panel) and  $0.4$  (the bottom panel). We show the observed values of  $I(\text{He II})/I(\text{H}\beta) \sim 0.004 - 0.07$  for the He II nebulae in the Cartwheel galaxy (Mayya et al. 2023) by the blue shaded

region. The results are generally consistent with what we might have expected from Figure 8: both the  $[\text{Fe}/\text{H}] = 0.0$  and  $-1.0$  models go through  $\sim 1$  Myr-long intervals where the line intensity ratio is in the observed band, independent of rotation rate or gas density, while  $[\text{Fe}/\text{H}] = -2.0$  remains in this range for such longer duration only for rapid rotation, and is well below it for zero rotation. For all these models, the maximum of  $I(\text{He II})/I(\text{H}\beta)$  occurs at the time at which the most massive stars ( $\gtrsim 70 M_{\odot}$ ) are in their WR phases, at stellar ages of  $\sim 3 - 4$  Myr.

We can understand the physical origins of several features of these plots. First, for the non-rotating case we notice that the  $[\text{Fe}/\text{H}] = -1$  case yields the highest  $I(\text{He II})/I(\text{H}\beta)$  ratios and the longest duration within the  $\sim 0.004 - 0.07$  characteristic of observed He II-emitting nebulae. This occurs because at  $[\text{Fe}/\text{H}] = -1$  represents the optimal compromise between two effects: at high metallicity the surface opacity is too high to produce many He II-ionizing photons, while at low metallicity the mass loss rate is too low to expose the stellar core and produce high  $T_{\text{eff}}$ ; the  $[\text{Fe}/\text{H}] = -1$  does the best job of balancing these two effects, producing a surface temperature that is enough and a surface opacity that is low enough to maximize He II-ionizing photon production. For rapidly rotating stars, by contrast, high metallicity is not needed to produce high mass loss due to the rotation enhanced mass loss rates and rotational mixing described above; consequently, for the rapidly rotating case, we find that time spent at high  $I(\text{He II})/I(\text{H}\beta)$  increases monotonically as metallicity decreases.

#### 3.2.2. Line equivalent widths

In addition to examining line ratios, we can also check that our clumpy wind models yield line equivalent widths (EWs) that are consistent with observations. We specifically check the widths of the He II, H $\beta$ , and blue bump (BB) lines. To calculate the EWs of the He II and H $\beta$  lines, we determine the line fluxes by integrating the nebular plus stellar spectra output by `CLOUDY` over  $40 \text{ \AA}$ -wide bands centered at  $4685.5$  and  $4865 \text{ \AA}$  respectively. We obtain the corresponding continuum fluxes for these two lines by integrating over regions on the either side of the line of interest chosen to contain no or only very weak lines; for the He II line we obtain the continuum level by integrating the spectra from  $4760 - 4840 \text{ \AA}$  and from  $4540 - 4620 \text{ \AA}$  and averaging the two results, while for H $\beta$  line we integrate from  $4885 - 4935 \text{ \AA}$  and  $4790 - 4840 \text{ \AA}$  and average the results. We calculate the BB line flux by integrating the spectra from  $4570 - 4740 \text{ \AA}$ , and the corresponding continuum flux as the average of results obtained by integrating the spectrum over  $50 \text{ \AA}$  windows centred at  $4525 \text{ \AA}$  and  $4905 \text{ \AA}$ , corresponding to the red and blue sides of the BB feature; our procedure here follows that of Mayya et al. (2023).

We show the time evolution of the EWs for our three lines of interest in Figure 10, Figure 11, and Figure 12, respectively. Examining these figures, we see that during the epochs from  $\approx 3 - 4$  Myr when our models predict  $I(\text{He II})/I(\text{H}\beta)$  ratios sufficiently large to match observations, the typical EWs of the He II  $\lambda 4686$ , H $\beta$ , and BB lines in the range  $\sim 0.1 - 3.5 \text{ \AA}$ ,  $\sim 20 - 300 \text{ \AA}$ , and  $\sim 2 - 10 \text{ \AA}$ , respectively. Exact values vary with metallicity and rotation rate, but these values are in good agreement with the typical ranges found in He II-emitting regions by Mayya et al. (2020, 2023). We therefore conclude that, not only do clumpy wind models for single stars produce  $I(\text{He II})/I(\text{H}\beta)$  ratios similar to observed values, they also reproduce the observed line-to-continuum ratios in these two lines, as well as in the BB feature.

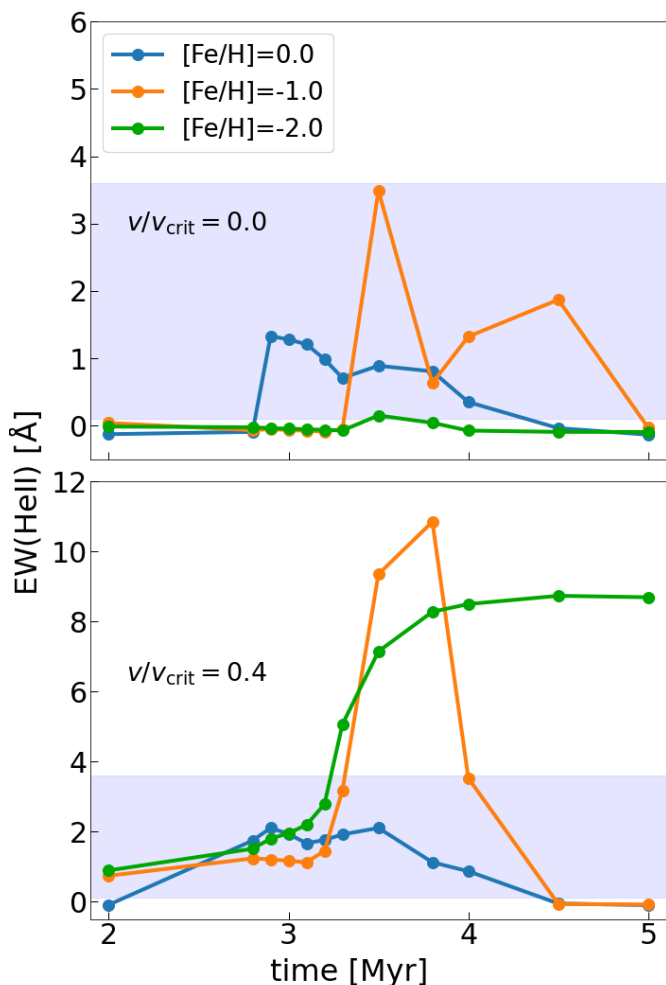


Fig. 10. Same as Figure 9, but now showing He II EW.

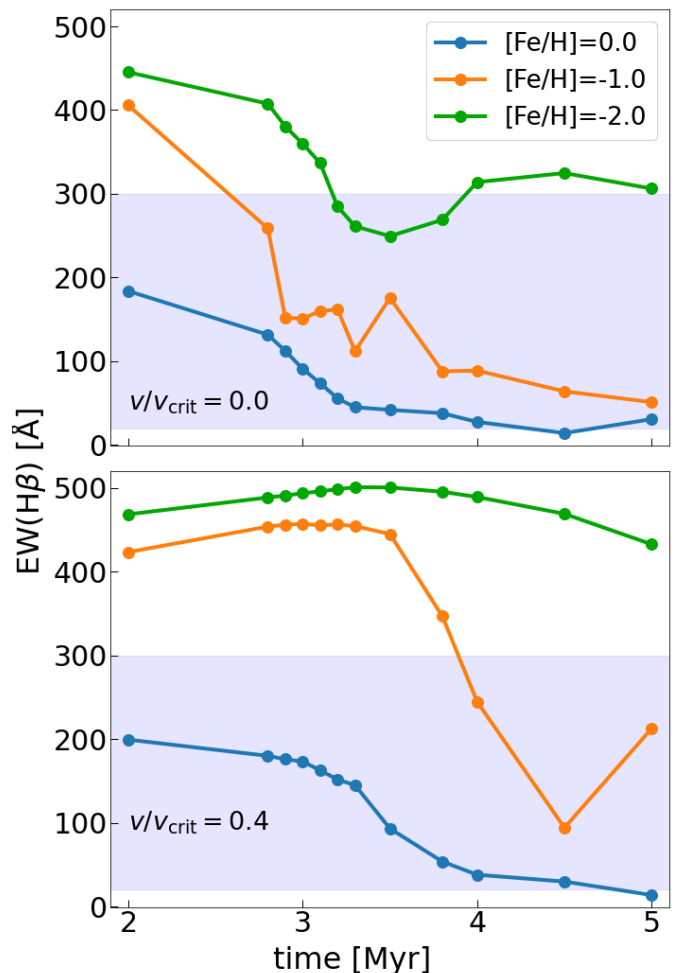


Fig. 11. Same as Figure 10, but for H $\beta$ .

### 3.2.3. Dependence on wind clumpiness

Thus far we have focused on our highest-clumping case, demonstrating that it yields line ratios and EWs that are in very good agreement with observations. We now return to our other two cases, no clumping, laminar winds and intermediate clumping, using our full pipeline to predict  $I(\text{He II})/I(\text{H}\beta)$  ratios and EW for the He II line exactly as we have for the highly-clumped case. We show the results in Figure 13 and Figure 14, respectively.

We find that for both Solar and 1/10th Solar metallicity, only the highly-clumped and porous winds, that is on the verge of optically thin scenario, can produce the observed  $I(\text{He II})/I(\text{H}\beta)$  ratio  $\sim 0.004 - 0.07$ , but that for the most metal-poor case,  $[\text{Fe}/\text{H}] = -2.0$  and rapidly rotating stars,  $v/v_{\text{crit}} = 0.4$ , even partially clumpy winds reproduce the observed  $I(\text{He II})/I(\text{H}\beta)$  ratio. This case, while it has a lower He II EW than the highly clumped case, nonetheless reaches EWs of  $\approx 4 \text{ \AA}$  at the  $\approx 3 - 5 \text{ Myr}$  ages when the  $I(\text{He II})/I(\text{H}\beta)$  ratio is high, well within the observed range for He II-emitters.

We therefore conclude that the combination of efficient rotation-driven CHE (for stars  $\geq 90 M_{\odot}$ ), mass-loss, and low atmospheric opacity in this case is sufficient to produce enough He II-ionizing photons to match observations even if the stellar surface is partly blocked by a semi-opaque wind.

## 4. Discussions and conclusions

The origin of nebular He II emission in star-forming galaxies remains an unresolved problem. The line is powered by the recombination of He $^{++}$ , production of which requires photons with energies  $\geq 54.4 \text{ eV}$ , which are thought to be difficult to produce with conventional single stellar populations. The challenge of explaining the production site of the required photons has led to a number of proposals, including photoionization of He $^{+}$  by binary stellar populations or by compact objects such as HMXBs and ULXs, shock-driven ionization, and hidden AGNs. By contrast, ionization by single massive and/or Wolf-Rayet (WR) stars has often been dismissed as a possibility because their He II ionizing photon production rates were thought to be too low.

However, the stellar models that were the basis for this conclusion have a number of limitations. They treated stellar winds as spherically homogeneous and optically thick, at odds with modern observational constraints. They assumed that the responsible stars were non-rotating, contrary to theoretical expectations that massive stars should be born with high rotation rates (Rosen et al. 2012). In this paper we remove these limitations and revisit the single WR channel as a possible source for the nebular He II emission, using a dense grid of massive stellar evolution models at a range of metallicities and rotation rates, coupled to multiple possible treatments of WR wind clumping.

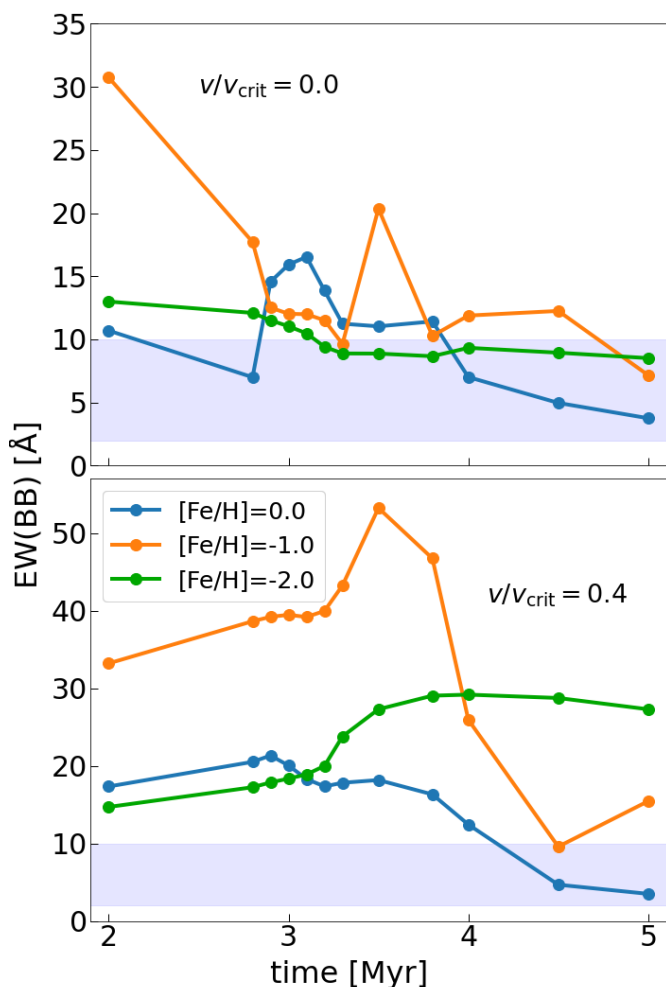


**Fig. 12.** Same as Figure 10 and Figure 11, but for the blue bump (BB) line-blend feature.

We find that varying our treatment of clumping in extended WR atmospheres lead to dramatic variations in predicted He II-ionizing photon budgets, with models that assume highly clumped winds that expose most of the stellar surface yielding factor of 20 increases in production of photons beyond the He<sup>+</sup> ionization edge compared to traditional models where winds are treated as laminar and optically thick. This enhanced production of hard photons occurs for stellar populations with ages of  $\approx 3-5$  Myr, corresponding to the time at which the most massive stars,  $\gtrsim 70 M_{\odot}$ , enter the WR phase for  $[\text{Fe}/\text{H}] \gtrsim -2.0$ .

During this period of enhanced hard photon production, nebular modelling with CLOUDY reveals that nebulae powered by stellar populations with highly-clumped winds experience  $\sim 1-2$  Myr periods where their ratio of He II  $\lambda 4686$  to H $\beta$  line luminosities reaches the large values,  $I(\text{He II})/I(\text{H}\beta) \sim 0.004-0.07$ , observed in local He II-emitting regions. During this periods the equivalent widths of the He II, H $\beta$ , and blue bump lines are also comparable to observed values – a few Angstroms, a few hundred Angstroms, and a few tens of Angstroms, respectively. These periods when the predicted nebular emission closely matches what we observe occur for all metallicities and stellar rotation rates if winds are highly clumped. If we treat WR winds as moderately clumped elevated  $I(\text{He II})/I(\text{H}\beta)$  ratios and He II equivalent widths still occur for metal-poor, rapidly rotating stellar populations ( $[\text{Fe}/\text{H}] = -2$ ,  $v/v_{\text{crit}} = 0.4$ ), but not for more metal-poor or

non-rotating ones, while for a conventional model using laminar winds there are no periods of elevated  $I(\text{He II})/I(\text{H}\beta)$  for any of the metallicities or rotation rates we have considered, consistent with earlier work.

We therefore conclude that earlier estimates that single stars with moderate rotation rates,  $v/v_{\text{crit}} \lesssim 0.5$  could not be the drivers of nebular He II emission are incorrect, since this conclusion holds only if we assume that these stars have laminar winds. On the contrary, *single WR stars with highly clumpy to partially clumpy winds are a strong candidate for driving the nebular He II emission seen in both local and high-redshift galaxies.*

Our findings have important implications, particularly at high redshifts. Massive stars in metal-poor environments are typically expected to be moderately to rapidly rotating, with  $v/v_{\text{crit}} \gtrsim 0.4$  (Rosen et al. 2012), and high-redshift galaxies may also have IMFs more abundant in massive stars (e.g., Sharda & Krumholz 2022; van Dokkum & Conroy 2024). These combined factors likely result in a greater abundance of massive, rotating stars in the early Universe, facilitating the contribution of single massive stars as significant sources of He II emission. This may explain the increasing abundance of He II-emitters in the early Universe, and may have further implications for He II reionization.

*Acknowledgements.* Authors thank Daniel Schaerer and Anastasios Fragkos for the insightful discussions on the current challenges of nebular He II emission. Authors also thank Andrea Ferrara for extremely useful discussions on the He II emissions at high-redshift galaxies. AR gratefully acknowledges the support from Andrea Ferrara’s Italian funding scheme “The quest for the first stars” (Cod. 2017T4ARJ5\_001). SS and AP also acknowledge the support from the Italian funding scheme “The quest for the first stars” (Cod. 2017T4ARJ5\_001). MRK acknowledges support from the Australian Research Council through its *Laureate Fellowship* scheme, award FL220100020. GM and SE have received funding from the European Research Council (ERC) under the European Union’s Horizon 2020 research and innovation programme (grant agreement No 833925, project STAREX). JSV acknowledges support from STFC (Science and Technology Facilities Council) funding under grant number ST/V000233/1. AS is supported by the German Deutsche Forschungsgemeinschaft (DFG) under Project-ID 445674056 (Emmy Noether Research Group SA4064/1-1, PI Sander). The simulation data for this research/project were produced with the assistance of resources and services from the Scuola Normale Superiore’s Center for High Performance Computing (CHPC), and the National Computational Infrastructure (NCI)’s supercomputer Gadi, supported by the Australian Government (award jh2). Additional software used include SciPy (Virtanen et al. 2020), matplotlib (Hunter 2007), and NumPy (Harris et al. 2020).

## Data availability

The data underlying this article will be shared on request to the corresponding author (AR).

## References

- Berg, D. A., Erb, D. K., Auger, M. W., Pettini, M., & Brammer, G. B. 2018, *ApJ*, 859, 164  
Cassata, P., Le Fèvre, O., Charlot, S., et al. 2013, *A&A*, 556, A68  
Chabrier, G. 2003, *PASP*, 115, 763  
Chatzikos, M., Bianchi, S., Camilloni, F., et al. 2023, *Rev. Mexicana Astron. Astrofis.*, 59, 327  
Chené, A.-N., St-Louis, N., Moffat, A. F. J., & Gayley, K. G. 2020, *ApJ*, 903, 113  
Choi, J., Dotter, A., Conroy, C., et al. 2016, *ApJ*, 823, 102  
da Silva, R. L., Fumagalli, M., & Krumholz, M. 2012, *ApJ*, 745, 145  
Dopita, M. A. & Sutherland, R. S. 1996, *ApJS*, 102, 161  
Ekström, S., Georgy, C., Eggenberger, P., et al. 2012, *A&A*, 537, A146  
Eldridge, J. J., Stanway, E. R., Xiao, L., et al. 2017, *PASA*, 34, e058  
Eversberg, T., Lépine, S., & Moffat, A. F. J. 1998, *ApJ*, 494, 799  
Feltre, A., Charlot, S., & Gutkin, J. 2016, *MNRAS*, 456, 3354  
Friend, D. B. & Abbott, D. C. 1986, *ApJ*, 311, 701  
Fullerton, A. W., Massa, D. L., & Prinja, R. K. 2006, *ApJ*, 637, 1025  
Georgy, C., Ekström, S., Eggenberger, P., et al. 2013, *A&A*, 558, A103  
Georgy, C., Ekström, S., Meynet, G., et al. 2012, *A&A*, 542, A29  
Götberg, Y., de Mink, S. E., Groh, J. H., et al. 2018, *A&A*, 615, A78

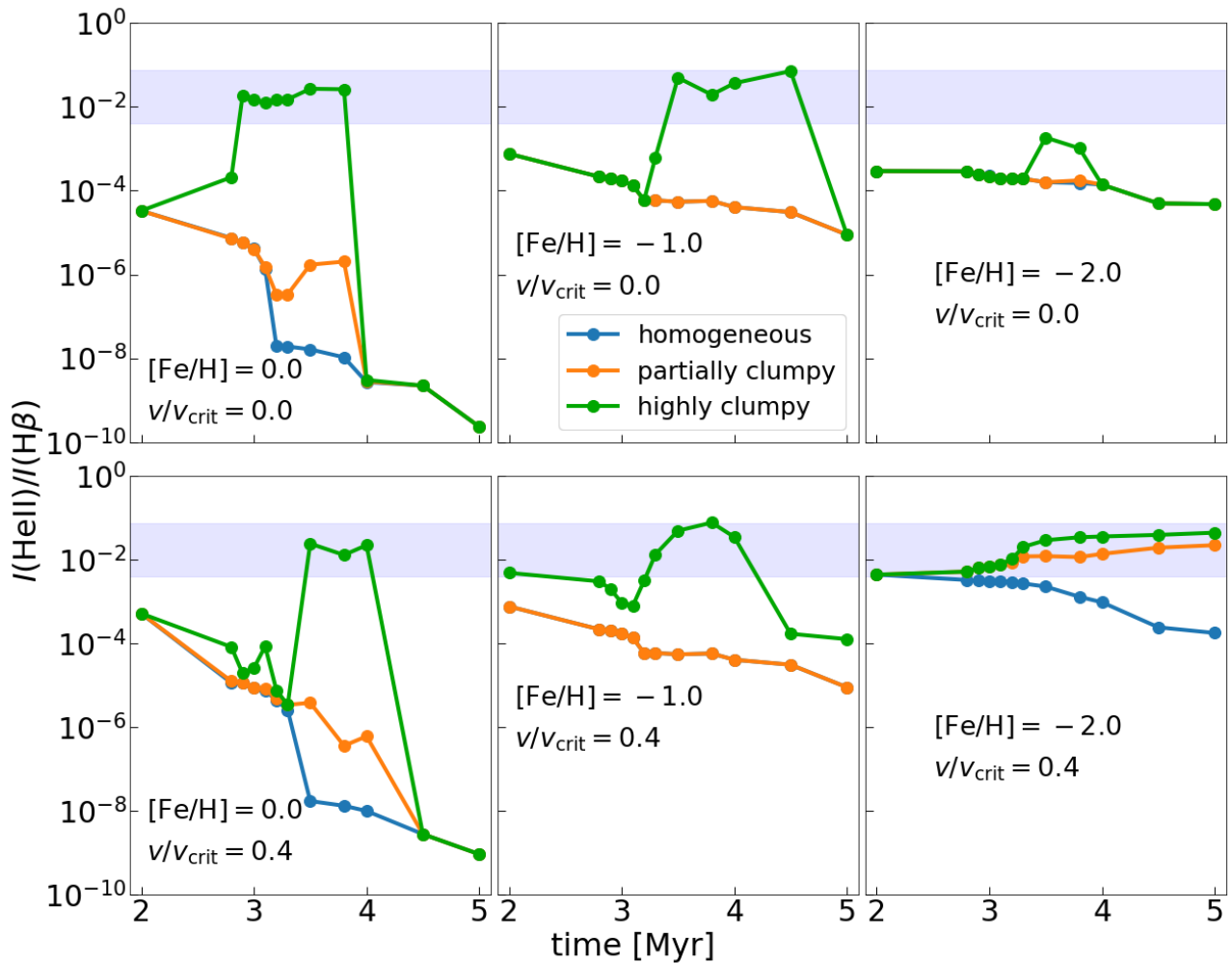


**Fig. 13.** Same as Figure 9, except here different colors corresponds to different wind morphology, ranging from optically thick and homogeneous winds (blue) to partially clumpy (orange) to highly clumpy, porous, on the verge of optically thin winds (green). Each panel shows a different combination of metallicity and stellar rotation rate: columns show, from left to right,  $[\text{Fe}/\text{H}] = 0, -1, -2$ , while rows show  $v/v_{\text{crit}} = 0$  (top) and 0.4 (bottom).

- Götberg, Y., de Mink, S. E., Groh, J. H., Leitherer, C., & Norman, C. 2019, *A&A*, 629, A134
- Grasha, K., Roy, A., Sutherland, R. S., & Kewley, L. J. 2021, *ApJ*, 908, 241
- Grosdidier, Y., Moffat, A. F. J., Blais-Ouellette, S., Joncas, G., & Acker, A. 2001, *ApJ*, 562, 753
- Guseva, N. G., Izotov, Y. I., & Thuan, T. X. 2000, *ApJ*, 531, 776
- Harris, C. R., Millman, K. J., van der Walt, S. J., et al. 2020, *Nature*, 585, 357
- Hillier, D. J. & Miller, D. L. 1998, *ApJ*, 496, 407
- Hunter, J. D. 2007, *Computing in Science and Engineering*, 9, 90
- Izotov, Y. I. & Thuan, T. X. 2004, *ApJ*, 602, 200
- Izotov, Y. I., Thuan, T. X., & Privon, G. 2012, *MNRAS*, 427, 1229
- James, B. L., Berg, D. A., King, T., et al. 2022, *ApJS*, 262, 37
- Kehrig, C., Oey, M. S., Crowther, P. A., et al. 2011, *A&A*, 526, A128
- Kehrig, C., Vílchez, J. M., Guerrero, M. A., et al. 2018, *MNRAS*, 480, 1081
- Kehrig, C., Vílchez, J. M., Pérez-Montero, E., et al. 2015, *ApJ*, 801, L28
- Kehrig, C., Vílchez, J. M., Pérez-Montero, E., et al. 2016, *MNRAS*, 459, 2992
- Krumholz, M. R., Fumagalli, M., da Silva, R. L., Rendahl, T., & Parra, J. 2015, *MNRAS*, 452, 1447
- Kudritzki, R. P., Pauldrach, A., Puls, J., & Abbott, D. C. 1989, *A&A*, 219, 205
- Lamers, H. J. G. L. M. & Cassinelli, J. P. 1999, *Introduction to Stellar Winds*
- Langer, N. 1998, *A&A*, 329, 551
- Leitherer, C., Schaerer, D., Goldader, J. D., et al. 1999, *ApJS*, 123, 3
- Lejeune, T., Cuisinier, F., & Buser, R. 1997, *A&AS*, 125, 229
- Lépine, S. & Moffat, A. F. J. 2008, *AJ*, 136, 548
- López-Sánchez, Á. R. & Esteban, C. 2010, *A&A*, 516, A104
- Mayya, Y. D., Carrasco, E., Gómez-González, V. M. A., et al. 2020, *MNRAS*, 498, 1496
- Mayya, Y. D., Plat, A., Gómez-González, V. M. A., et al. 2023, *MNRAS*, 519, 5492
- Moens, N., Poniatowski, L. G., Hennicker, L., et al. 2022, *A&A*, 665, A42
- Moffat, A. F. J., Drissen, L., Lamontagne, R., & Robert, C. 1988, *ApJ*, 334, 1038
- Nanayakkara, T., Brinchmann, J., Boogaard, L., et al. 2019, *A&A*, 624, A89
- Nicholls, D. C., Sutherland, R. S., Dopita, M. A., Kewley, L. J., & Groves, B. A. 2017, *MNRAS*, 466, 4403
- Nugis, T. & Lamers, H. J. G. L. M. 2000, *A&A*, 360, 227
- Patrício, V., Richard, J., Verhamme, A., et al. 2016, *MNRAS*, 456, 4191
- Pauldrach, A., Puls, J., & Kudritzki, R. P. 1986, *A&A*, 164, 86
- Pauldrach, A. W. A., Hoffmann, T. L., & Lennon, M. 2001, *A&A*, 375, 161
- Plat, A., Charlot, S., Bruzual, G., et al. 2019, *MNRAS*, 490, 978
- Puls, J., Markova, N., Scuderi, S., et al. 2006, *A&A*, 454, 625
- Rémy-Ruyer, A., Madden, S. C., Galliano, F., et al. 2014, *A&A*, 563, A31
- Rosen, A. L., Krumholz, M. R., & Ramirez-Ruiz, E. 2012, *ApJ*, 748, 97
- Roy, A., Dopita, M. A., Krumholz, M. R., et al. 2021, *MNRAS*, 502, 4359
- Roy, A., Sutherland, R. S., Krumholz, M. R., Heger, A., & Dopita, M. A. 2020, *MNRAS*[arXiv:1907.07666]
- Sander, A. A. C., Lefever, R. R., Poniatowski, L. G., et al. 2023, *A&A*, 670, A83
- Sander, A. A. C., Vink, J. S., & Hamann, W. R. 2020, *MNRAS*, 491, 4406
- Saxena, A., Pentericci, L., Mirabelli, M., et al. 2020a, *A&A*, 636, A47
- Saxena, A., Pentericci, L., Schaerer, D., et al. 2020b, *MNRAS*, 496, 3796
- Schaerer, D. 2002, *A&A*, 382, 28
- Schaerer, D. 2003, *A&A*, 397, 527
- Schaerer, D., Fragos, T., & Izotov, Y. I. 2019, *A&A*, 622, L10
- Schaller, G., Schaerer, D., Meynet, G., & Maeder, A. 1992, *A&AS*, 96, 269
- Schumann, J. D. & Seggewiss, W. 1975, in *Variable Stars and Stellar Evolution*, ed. V. E. Sherwood & L. Plaut, Vol. 67, 299
- Senchyna, P., Stark, D. P., Mirocha, J., et al. 2020, *MNRAS*, 494, 941
- Sharda, P. & Krumholz, M. R. 2022, *MNRAS*, 509, 1959
- Shirazi, M. & Brinchmann, J. 2012, *MNRAS*, 421, 1043

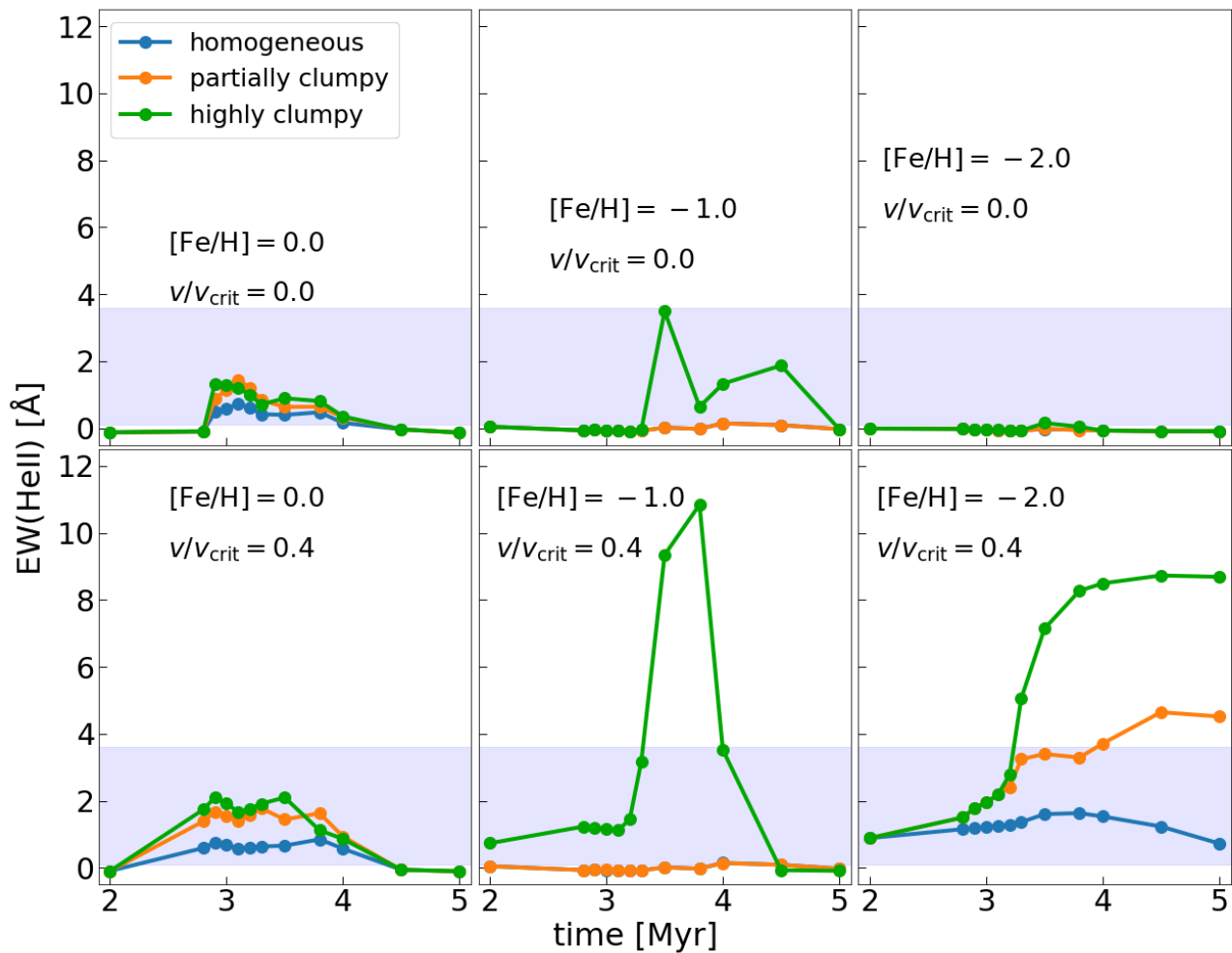


**Fig. 14.** Same as Figure 10, except for here we show the comparison for the three atmosphere morphology. Here the three metallicity cases are in three different panels:  $[\text{Fe}/\text{H}] = 0.0$  (leftmost panels),  $-1.0$  (middle panels), and  $-2.0$  (rightmost panels).

Sixtos, A., Wofford, A., Sander, A. A. C., & Peimbert, A. 2023, MNRAS, 519, 5656

Sobral, D., Matthee, J., Brammer, G., et al. 2019, MNRAS, 482, 2422

Stanway, E. R. & Eldridge, J. J. 2019, A&A, 621, A105

Stark, D. P. 2016, ARA&A, 54, 761

Székési, D., Langer, N., Yoon, S.-C., et al. 2015, A&A, 581, A15

Thuan, T. X. & Izotov, Y. I. 2005, ApJS, 161, 240

Tumlinson, J. & Shull, J. M. 2000, ApJ, 528, L65

van Dokkum, P. & Conroy, C. 2024, ApJ, 973, L32

Vázquez, G. A. & Leitherer, C. 2005, ApJ, 621, 695

Vink, J. S., de Koter, A., & Lamers, H. J. G. L. M. 2001, A&A, 369, 574

Virtanen, P., Gommers, R., Oliphant, T. E., et al. 2020, Nature Methods, 17, 261

Visbal, E., Haiman, Z., & Bryan, G. L. 2015, MNRAS, 450, 2506

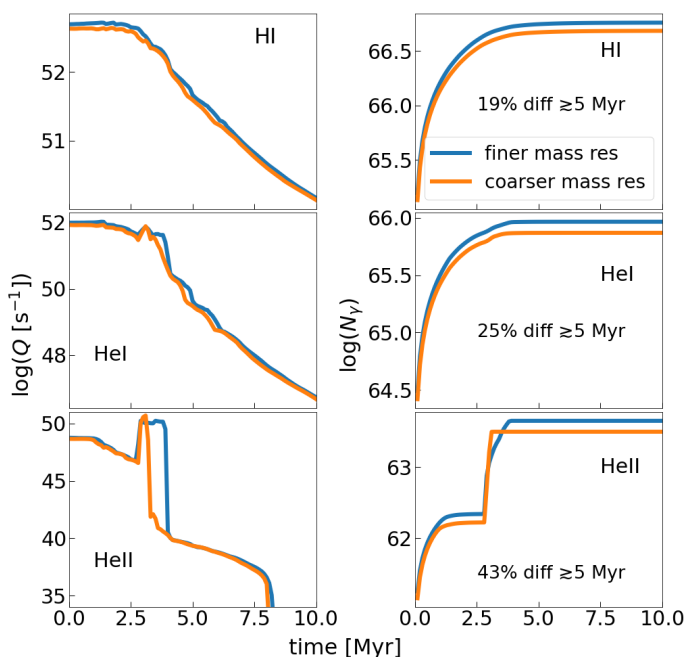


**Fig. A.1.** Same as Figure 1, but now comparing the results generated using MIST models (blue, finer mass resolution) and Geneva models (orange, coarser mass resolution). For both sets of models we show the case of highly-clumped, close to optically-thin winds.

## Appendix A: On the importance of mass resolution

As discussed in the main text, we use MIST tracks in part because of the high mass resolution they offer at the high mass end of the IMF. To demonstrate why this is important, we compare MIST results to results generated using Geneva stellar tracks<sup>7</sup> (Ekström et al. 2012; Georgy et al. 2013), which are the most widely used for massive stars but have much lower mass resolution at the upper end of the mass range; specifically, they include models at initial mass  $M = 60, 85$  and  $120 M_{\odot}$  only.

To demonstrate the importance of resolution, in Figure A.1 we show the time evolution of the H I, He I, and He II ionizing luminosities for highly-clumped, optically thin atmospheres computed using Geneva and MIST-I stellar tracks, holding all other parameters at the same values used in Figure 1. The blue line shown here for the MIST-I models is identical to the highly-clumped case shown in Figure 1. For the Geneva tracks we observe kinks in the He I and He II ionizing luminosities as stars  $\gtrsim 70 M_{\odot}$  enter the WR phase, similar to the MIST results, but we find that this peak is substantially broader in time for the finer mass-resolution compared to the coarser one, resulting in cumulative differences of approximately 25% and 45% for He I and He II respectively, with a comparatively smaller difference in H I luminosities of  $\sim 20\%$  at  $\gtrsim 5$  Myr. The difference is not due to differences in the results for individual stars – the MIST and Geneva tracks at 60 and  $120 M_{\odot}$  are quite similar to one another, and differ in their predicted ionizing photon production by much less than the values shown in Figure A.1. Instead, the difference is simply a result of the need for far more interpolation across the mass range that produces WR stars in the lower-resolution Geneva tracks than for the higher-resolution MIST ones.

## Appendix B: Dependence on initial abundance

As discussed in subsection 2.1, for the main part of the paper we use MIST tracks, which assume Solar-scaled abundances. However, we find in subsection 3.1.3 that metallicity plays a crucial role in determining mass-loss rates, and consequently, the ionizing photon budgets, particularly for non-rotating stars, and it is therefore important to verify that these results do not change significantly if we adopt more realistic non-Solar-scaled abundances. For this purpose we compare the results from MIST to results generated using the Stromlo Stellar Tracks (SST; Grasha et al. 2021)<sup>8</sup>, focusing only on non-rotating tracks, since we have seen in subsection 3.1.3 that surface parameters are independent of metallicities for stars with  $v/v_{\text{crit}} = 0.4$ , and on metallicities  $[\text{Fe}/\text{H}] = -1$  and  $-2$ , since MIST and SST are nearly identical at Solar metallicity. We show the time evolution of the instantaneous and cumulative ionizing photon outputs for these cases in Figure B.1.

For softer photons (H I and He I), we see that MIST and SST produce similar results, with maximal percentage differences in cumulative photon luminosities of  $\sim 12.8\%$  and  $\sim 3.7\%$  for H I, and  $\sim 18\%$  and  $\sim 5\%$  for He I at  $[\text{Fe}/\text{H}] = -1$  and  $-2.0$ , respectively. However, the disparity increases for harder photons (He II), where the maximal differences reach  $\sim 155\%$  and  $\sim 68\%$  for  $[\text{Fe}/\text{H}] = -1$  and  $-2$ , respectively. While this difference is not negligible, it is also not as pronounced as those induced by other parameter choices, and in particular is much smaller than the effects of our choice of atmosphere model. We therefore conclude that our results remain robust regardless of the initial abundance distribution, and adopt the Solar-scaled abundance pattern throughout the main text.

<sup>7</sup> <https://www.unige.ch/sciences/astro/evolution/en/database/>

<sup>8</sup> Note that both MIST and SST have exactly same physics models and parameters, the only difference comes in their initial abundance setups.

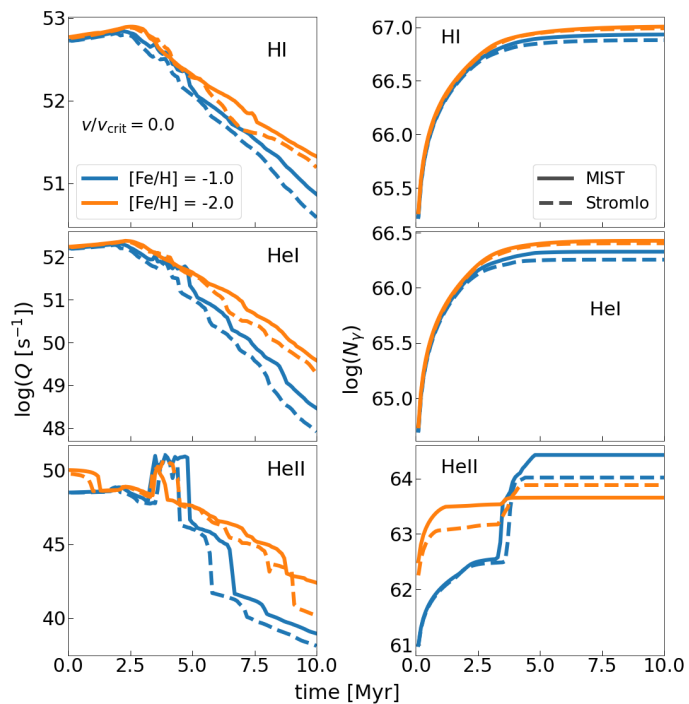


**Fig. B.1.** Same as Figure 1, but now comparing the results generated using MIST and Stromlo stellar tracks to show the dependence on initial metal abundances at a given metallicity. The tracks shown here are for two metallicities,  $[\text{Fe}/\text{H}] = -1$  and  $-2$ , and for non-rotating stars with highly-clumped, close to optically-thin winds.